crystals

MDPI

Article

Temperature-Dependent Effectiveness of Ti, Nb, Zr, and Y in Controlling Grain Growth of AISI 304 Austenitic Stainless Steel

Jaka Burja [1,2,3,*], Samo Tome [1,2] and Aleš Nagode [2]

[1] Institute of Metals and Technology, Lepi Pot 11, 1000 Ljubljana, Slovenia
[2] Faculty of Natural Sciences and Engineering, University of Ljubljana, Aškerčeva cesta 12, 1000 Ljubljana, Slovenia
[3] College of Industrial Engineering, Mariborska Cesta 2, 3000 Celje, Slovenia
* Correspondence: jaka.burja@imt.si

Abstract

Crystal grain size control in steel is critical for achieving mechanical properties. This study investigates the effectiveness of microalloying with titanium, niobium, zirconium, and yttrium to inhibit grain growth with the pinning effect. The comparison of selected microalloying elements in the exact same conditions is crucial for understanding their effect and is novel. Hot-rolled samples were annealed across a wide range of temperatures (1050 to 1200 °C) for up to eight hours. Microstructural analysis confirmed the presence of stable precipitates and non-metallic inclusions such as Nb(C,N), Ti(C,N), ZrO_2, and Y_2O_3 acting as obstacles to grain boundary migration. All microalloying elements significantly outperformed the reference steel, but their effectiveness was highly dependent on the annealing temperature. Titanium was the most effective inhibitor at lower temperatures (1050 °C), while zirconium maintained control up to 1150 °C. Critically, at the highest temperature of 1200 °C, only the yttrium-alloyed steel retained a fine-grain structure, demonstrating superior thermal stability. Niobium, conversely, only showed a minimal effect at 1050 °C, though this grade also exhibited the highest hardness (up to 165 HB) due to precipitation hardening. The kinetics of grain growth were successfully modeled using the Arrhenius-type Sellars–Whiteman equation, accurately describing the behavior for up to four hours of annealing. The findings provide critical insight for selecting optimal microalloying strategies based on maximum operating temperature.

Keywords: microalloying; grain growth; annealing; austenite

Academic Editor: José L. García

Received: 15 October 2025
Revised: 27 October 2025
Accepted: 28 October 2025
Published: 29 October 2025

Citation: Burja, J.; Tome, S.; Nagode, A. Temperature-Dependent Effectiveness of Ti, Nb, Zr, and Y in Controlling Grain Growth of AISI 304 Austenitic Stainless Steel. *Crystals* **2025**, *15*, 931. https://doi.org/10.3390/cryst15110931

1. Introduction

Steel properties are heavily influenced by crystal grain size; smaller grains enhance strength and toughness by providing more grain boundaries to impede dislocation movement. A coarse crystal grain structure in steel is generally undesirable. Larger crystal grains mean fewer boundaries, making the material less resistant to deformation and more prone to failure. In general, coarse crystal grains result in lower hardness, yield strength, ultimate strength, fatigue strength, impact toughness, and fracture toughness. [1–6]. Crystal grain growth in steels occurs at high temperatures, either during annealing, welding, hot forming, heating to quenching temperature, etc. In general, grain growth is defined by the reduction in total grain boundary area [7–11]. The driving force behind this is the minimization of the interfacial energy of the grains. Therefore, a larger amount of grain boundaries, as found in fine-grained materials, results in a larger driving force for grain growth. So larger, more thermodynamically stable grains grow at the expense of smaller, less stable grains [10,12,13] and mitigate the grain growth by introducing obstacles on the grain boundaries that produce a pinning effect. These obstacles are particles that are either precipitates or non-metallic inclusions that are stable at a given temperature. Carbonitride precipitates are typically utilized for stopping grain growth. Special carbonitride and nitride elements that form high-temperature stable precipitates are added in small quantities, typically below 0.1 wt.%. Microalloying elements are usually titanium, niobium, vanadium and aluminum [6,14–19]. They, however, impede grain growth in two ways: by solute drag, and by forming fine precipitates, such as carbides, nitrides and oxides, which are dispersed along the grain boundary [15–18]. When the steel is exposed to high temperatures, for example 1200 °C, the equilibrium dissolution temperature for most carbonitrides is surpassed, and they dissolve into the steel matrix. With no particles pinning the grain boundary, it continues to grow unimpeded. However, as the temperature drops, so does the solubility of the carbonitrides. Thus, they precipitate out of solid solution [20–23]. When a grain boundary comes into contact with an incoherent particle, the overall area of the grain boundary is reduced, due to the particle occupying that area. However, when the grain boundary begins to migrate beyond the particle, a new grain boundary needs to form. This grain boundary pinning, also known as the Zenner pinning, notes that the pinning force is determined by the volume fraction and size of the pinning particles. Coherent precipitates also significantly impede grain boundary migration. When a grain boundary comes into contact with the coherent particle, the area of contact switches to an incoherent interface, thus increasing the surface energy. If the temperature is high enough, the precipitated particles may begin to coarsen, reducing their pinning effect, or may dissolve into the solid solution [24–27]. Proper selection of alloying elements can impede grain growth at a given annealing temperature, thereby increasing the mechanical properties of the steel. Moreover, the finely dispersed particles increase the mechanical properties of the steel at room temperature [28–31]. Microalloying elements have a limited temperature range, as the temperature increases the particles start to dissolve in the matrix, this eliminates their grain growth reduction ability. This is especially true when heating up steel for hot forming temperatures that typically exceed 1000 °C, as they can reach above 1200 °C.

Austenitic stainless steels are widely used because of their excellent corrosion resistance, weldability and good workability [32,33]. The austenitic stainless steels do not undergo austenite to ferrite transformation during cooling. This limits grain refining mostly to the processes of plastic deformation, such as hot-rolling. The small grain size is an important factor for the improvement of mechanical, while the impact on corrosion resistance is not straightforward [34]. Grain growth occurs during high temperature annealing. Given that grain size has a large effect on material properties such as strength, toughness and hardness, grain growth is typically undesired [7,35]. In high strength low alloyed steels microalloying is employed to prevent such growth at high temperatures [36–42]. Elements that form high temperature stable precipitates, such as titanium, niobium, vanadium and aluminum among others are typically used.

In this study the grain boundary pinning effect of microalloying elements titanium, niobium, zirconium and yttrium was investigated at different annealing temperatures. To ensure that the actual grains that grow during high temperature annealing are observed, an austenitic stainless steel AISI 304 that has no phase transformations during cooling was used. The microalloying elements in the study form precipitates and non-metallic inclusions that are stable at different temperatures, as was analyzed by CALPHAD method.

2. Materials and Methods

The influence of microalloying elements on the grain growth of austenite was observed on samples made from AISI 304 steel, samples were alloyed with microalloying elements. We prepared samples with five different compositions: 304-0, which was the reference sample (without additional alloying elements); 304-Ti, containing 0.013 wt.% titanium; 304-Nb, containing 0.08 wt.% niobium; 304-Zr, containing 0.003 wt.% zirconium; and 304-Y, which had 0.013 wt.% yttrium. The composition of AISI 304 steel is given in Table 1.

Table 1. Composition of AISI 304 steel in wt.%.

C	Si	Mn	S	Cr	Ni	Cu	Mo	N
0.022	0.43	1.8	0.022	18.4	9.2	0.14	0.15	0.017

2.1. Melting and Casting

For titanium alloying, we used the ferroalloy FeTi, which contained 70 wt.% titanium. Niobium was alloyed with the ferroalloy FeNb, which contained 65 wt.% niobium, while zirconium and yttrium were alloyed using pure metals. Table 2 shows the mass of the 304 steel ingots charged into the furnace, and the masses of the alloying additions.

Table 2. Mass of 304 steel charge.

Batch Name	Mass of Steel Charge (kg)	Alloying Addition	Mass of Addition (g)
304-0	8.30	/	/
304-Ti	8.23	FeTi (70 mas. %)	6
304-Nb	8.30	FeNb (65 mas. %)	12
304-Zr	8.31	Zr	2.5
304-Y	8.00	Y	2.5

Melting was performed in a 45 kW vacuum induction melting furnace (VIM, Laebold Heraeus, Cologne, Germany) with a magnesite crucible. Table 3 provides the melting and stirring times.

Table 3. Melting and stirring times.

Batch	Melting Time (min)	Stirring Time After Addition (s)
1—304-0	78	/
2—304-Ti	36	20
3—304-Nb	31	90
4—304-Zr	29	20
5—304-Y	26	20

The charge was loaded into the crucible, the furnace chamber was evacuated, purged with nitrogen, re-evacuated, and then filled with Ar to the working pressure. The first batch was melted for a longer time to prevent the crucible from heating up too quickly, which could cause it to crack. During melting, the argon pressure in the chamber was approximately 300 mbar. Alloying was carried out using a doser located above the chamber. Once the steel was completely molten, the alloying elements were added. Before pouring the melt into the mold, the pressure was increased to 500 mbar. The melt was poured from the crucible into the mold. After casting, we waited for solidification to occur and filled the chamber with argon to limit oxidation during cooling. After 15 min, the pressure in the chamber was equalized with the ambient pressure, and the chamber lid was opened using a hydraulic lift. The mold was removed, and the furnace was recharged with a new batch. The cross-section of the cast ingot is 60 mm × 60 mm. The ingot was 500 mm long, a 100 mm head section was cut off after it had completely cooled.

2.2. Hot Rolling

The ingots were charged into a hot furnace at 1150 °C and annealed for 30 min. After solution annealing was complete, the furnace was opened, one ingot was removed, and rolling began. The rolls of the rolling mill were heated with a gas burner to approximately 4000 °C. The ingots were rolled into stips in nine rolling passes. Table 4 provides the dimensions of the cross-sections before and after rolling.

Table 4. Dimensions of cast ingots and strips after rolling and relative cross-sectional deformation.

	Cross-Section Before Rolling (mm × mm)	Cross-Section After Rolling (mm × mm)	Reduction Ratio
304-0	60 × 60	21 × 69	2.48
304-Nb	60 × 60	20 × 70	2.57
403-Ti	60 × 60	20 × 71	2.53
304-Zr	60 × 60	19 × 72	2.63
304-Y	60 × 60	20 × 69	2.61

2.3. High Temperature Annealing

The samples were annealed at four temperatures: 1050, 1100, 1150, and 1200 °C. Since the samples were placed in a cold furnace, they were annealed for six different durations: after the furnace reached the set temperature, after half an hour, one hour, two hours, four hours, and eight hours. After annealing, the samples were quenched in water. Figure 1 schematically shows the process route for solid-state processing.

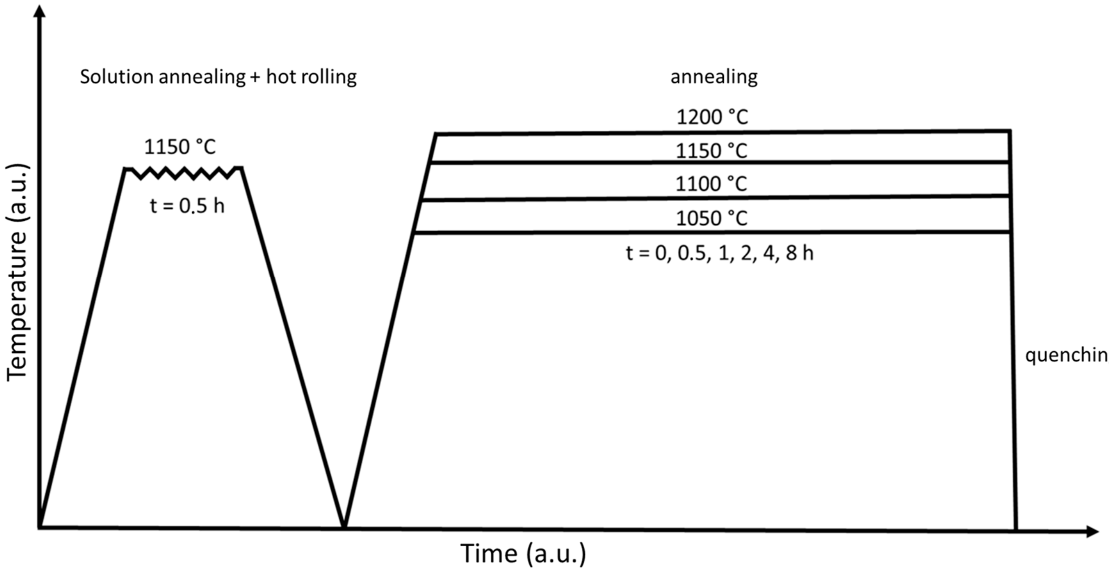

Figure 1. Schematic representation of the solid-state processing route.

2.4. Metallographic Sample Preparation

Due to exposure to high temperatures in an unprotected atmosphere, an oxide scale layer formed on the samples. The thickness of the scale was greater at higher temperatures and longer annealing times. The oxide scale was removed by rough grinding. At the same time, the edges of the samples were also ground to facilitate further preparation.

Sample cutting was performed on a Struers Labotom-3 machine (Struers ApS, Ballerup, Danmark). We used Struers 30A25 (Struers ApS, Ballerup, Danmark) cutting wheels for medium-soft iron alloys. After all samples were cut to an appropriate thickness, they were mounted in Multifast Bakelite mass using a Struers ProntoPress-20 machine (Struers ApS, Ballerup, Danmark). The samples were etched with aqua regia (10 mL glycerol, 15 mL HCl, and 5 mL HNO_3).

2.5. Measurement of Crystal Grain Size

Crystal grain sizes were measured according to the ASTM E112 method, in which the grain sizes were compared under 100× magnification on a light microscope with a diagram that shows the average crystal grain sizes. The sizes are designated from 00 to 15. These numbers were then converted to the average grain size. The samples were observed with a Nikon Mikrophot-FXA light microscope (Nikon, Tokyo, Japan).

2.6. Delta Ferrite Measurement

The delta ferrite measurements were carried out with a Fisher Feritscope MP30 (Fisher Scientific, Waltham, MA, USA), which uses a magnetic probe to measure the volume fraction of delta ferrite. Five measurements were taken for each sample. The Feritscope MP30 detects between 0.1 and 80 vol.% of delta ferrite in austenitic steel and has a maximum permissible measurement deviation of ± 0.4 vol.%, according to American Welding Society [43].

2.7. Chemical Analysis

Chemical analysis was performed using X-ray fluorescence spectrometry (XRF), and the chemical analysis of the basic elements in various metallic materials was performed by inductively coupled plasma optical emission spectrometry (ICP-OES) (Agilent 5800 VDV, Agilent Technologies, Santa Clara, CA, USA), CS analyzer (ELTRA CS800, Haan, Germany), and ON analyzer (ELTRA ON900, Haan, Germany).

2.8. Brinell Hardness Measurement

Sample hardness was measured on an Innovatest Nexus 3000 machine (Innovatest, Maastricht, The Netherlands). The measurements were performed according to the SIST EN 6506-1:2014 standard. Three measurements per sample were made using the ring-light method, with a 2.5 mm diameter tungsten carbide ball and a load of 187.5 kg.

2.9. Thermodynamic Analysis

For thermodynamic analysis of stable phases, we used the ThermoCalc 2017a software. The system was defined by the chemical composition of the alloys, and then the program plotted a diagram of the stable phase fraction as a function of temperature. We also calculated the fraction of stable phases and the chemical composition of the phases. For the calculations, we used the TCFE8: Steels/Fe-Alloys v8.1 database (Thermocalc Software AB, Solna, Sweden).

3. Results and Discussion

3.1. Chemical Analysis

The results of the chemical analyses are presented in Table 5, and the yield of alloying elements in Table 6. In addition to niobium, which had an 85% yield, the yields for titanium (25.5%), yttrium (43.3%), and zirconium (10%) were low. Due to the high oxygen content in the melt, the low yield can be attributed to the oxidation of the alloying elements in the melt.

Table 5. Chemical analysis of primary elements in various metallic materials by inductively coupled plasma optical emission spectrometry (ICP-OES) in wt.%.

	C	**Si**	**Mn**	**Cr**	**Ni**	**Cu**	**Mo**	**V**	**Ti**	**Nb**	**Zr**	**Y**	**O**	**N**
304-0	0.022	0.46	1.68	18.4	9.3	0.14	0.14	0.05	/	/	/	/	0.011	0.018
304-Nb	0.021	0.47	1.70	18.4	9.2	0.14	0.15	0.05	/	0.08	/	/	0.010	0.020
304-Ti	0.022	0.48	1.69	18.3	9.3	0.14	0.14	0.05	0.013	/	/	/	0.012	0.020
304-Y	0.019	0.47	1.69	18.3	9.0	0.14	0.14	0.05	/	/	/	0.013	0.008	0.019
304-Zr	0.021	0.48	1.76	18.9	9.5	0.14	0.14	0.05	/	/	0.003	/	0.010	0.019

Table 6. Amount of alloying elements in wt.%.

	Nb	**Ti**	**Y**	**Zr**
Theoretical addition	0.094	0.051	0.03	0.03
Final composition	0.08	0.013	0.013	0.003
Yield	85%	25.5%	43.3%	10%

3.2. Delta Ferrite Content

The highest delta ferrite values were found in the as-cast samples, where the ferrite content was between 9 and 10 vol.%. In the as-rolled condition, the ferrite content was between 4 and 7 vol.%. The as-cast ingots were annealed before rolling, which caused some of the delta ferrite to transform into austenite. The delta ferrite measurements for each composition in the as-cast and as-rolled conditions are given in Tables 7 and 8.

Table 7. Average delta ferrite content in as-cast samples, given in vol.%.

Sample	**304-0**	**304-Nb**	**304-Ti**	**304-Y**	**304-Zr**
δ-ferrite content	10.02	9.2	9.46	9.80	9.12

Table 8. Average delta ferrite content in as-rolled samples, given in vol.%.

Sample	**304-0**	**304-Nb**	**304-Ti**	**304-Y**	**304-Zr**
δ-ferrite content	6.78	6.42	6.08	4.80	4.06

In the annealed samples at temperatures of 1050, 1100, and 1150 °C, the initial delta ferrite content was, on average, higher (between 2 and 4.36 vol.%). As seen from Tables 9–12, at temperatures of 1100 and 1150 °C, the ferrite content rapidly decreased to values between 0.53 and 1.44 vol.% after just one hour. After one hour, the decomposition of delta ferrite proceeded much more slowly (the final delta ferrite content was between 0.23 and 1.25 vol.%). Due to the lower temperature at 1050 °C, the decomposition of delta ferrite was slower, as the content only reached between 0.95 and 1.34 vol.% after two hours. At 1200 °C, the initial delta ferrite content was the lowest among all temperatures (between 0.92 and 1.88 vol.%). Due to further transformation of delta ferrite with longer annealing times, we found the lowest content at four hours (between 0.17 and 0.31 vol.%). At eight hours, the delta ferrite content was so small that it could no longer be measured. It is worth noting that at all temperatures and the initial time, the niobium-alloyed steel had the highest delta ferrite content (from 1.88 to 4.36 vol.%). As the temperature increased, delta ferrite began to decompose into austenite. The results show that temperature has a greater influence on the ferrite content at shorter annealing times (one to two hours) than at longer times. At an annealing temperature of 1200 °C, the delta ferrite values were already low at the initial time, as most of the delta ferrite had already transformed during the heating of the samples to the mentioned temperature. Figure 2 shows the microstructure of delta ferrite in the as-cast, as-rolled, and annealed conditions

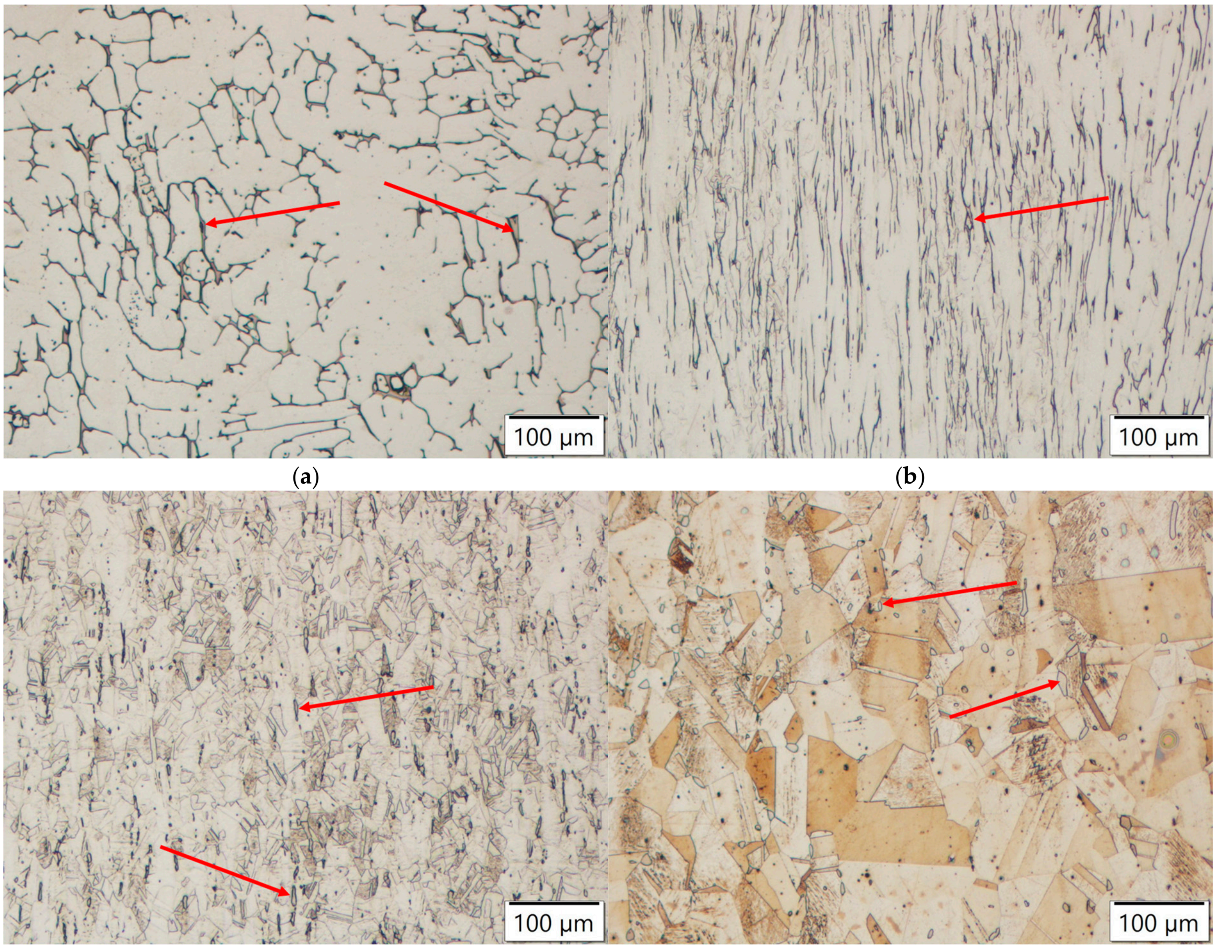

(a) (b)

(c) (d)

Figure 2. Microstructure of AISI 304 steel with marked delta ferrite (red arrows): (**a**) in as-cast state, (**b**) in as-rolled state, (**c**) quenched after the furnace reached 1050 °C, (**d**) annealed for four hours at 1200 °C.

Table 9. Average delta ferrite content by annealing time at 1050 °C, given in vol.%.

Time Annealed (h)	0	Nb	Ti	Y	Zr
0	1.98	4.04	3.74	2.44	2.11
0.5	1.66	2.58	1.92	1.7	1.72
1	1.82	2.2	2.22	1.86	1.4
2	0.95	1.34	1.24	1.07	1.03
4	0.73	0.84	0.70	0.52	0.44
8	0.38	0.44	0.28	0.37	0.27

Table 10. Average delta ferrite content by annealing time at 1100 °C, given in vol.%.

Time Annealed (h)	0	Nb	Ti	Y	Zr
0	3.62	4.3	3.86	3.86	2.56
0.5	2.8	2.74	2.22	2.34	1.82
1	0.74	1.4	1.5	1.36	1.11
2	1.03	1.12	0.64	1.45	0.75
4	0.97	0.45	0.28	0.75	0.31
8	0.91	0.64	0.23	1.25	0.23

Table 11. Average delta ferrite content by annealing time at 1150 °C, given in vol.%.

Time Annealed (h)	0	Nb	Ti	Y	Zr
0	3.16	4.36	2.78	3.34	2.34
0.5	2.44	2.78	1.76	1.29	1.46
1	1.12	0.93	0.62	0.79	0.53
2	0.34	0.80	0.40	0.37	0.51
4	0.35	0.47	0.30	1.02	0.29
8	0.31	0.36	0.63	0.92	0.39

Table 12. Average delta ferrite content by annealing time at 1200 °C, given in vol.%.

Time Annealed (h)	0	Nb	Ti	Y	Zr
0	1.56	1.88	1.01	0.94	0.92
0.5	0.94	1.32	0.75	0.60	0.35
1	0.71	0.77	0.63	0.30	0.59
2	0.49	0.29	0.26	0	0.29
4	0.20	0.31	0.23	0.17	0.22
8	0	0	0	0	0

Figure 3 shows a scanning electron microscope (SEM) image of delta ferrite, taken with a backscattered electron detector. The chemical analysis of the surface, performed with an energy-dispersive X-ray spectrometer (EDS), shows that in addition to austenite, delta ferrite is also present in the steel microstructure, as it contains a higher proportion of chromium and a lower proportion of nickel than austenite (Figure 3).

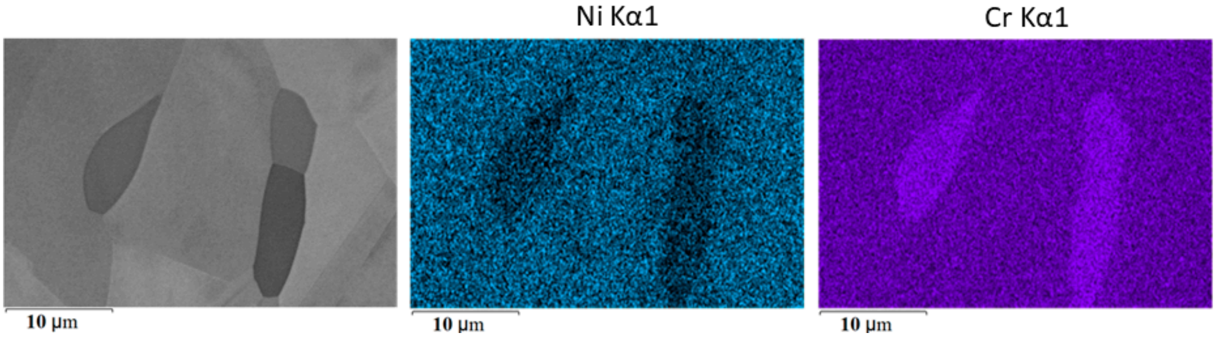

Figure 3. SEM image of delta ferrite and austenite and the distribution of nickel and chromium in the microstructure.

3.3. Precipitates and Non-Metallic Inclusions

Manganese sulfide and silicon oxide inclusions were found in the microstructure of the reference steel. Figure 4 shows the elemental composition of the surface with EDS analysis and the corresponding microstructure image taken with backscattered electrons.

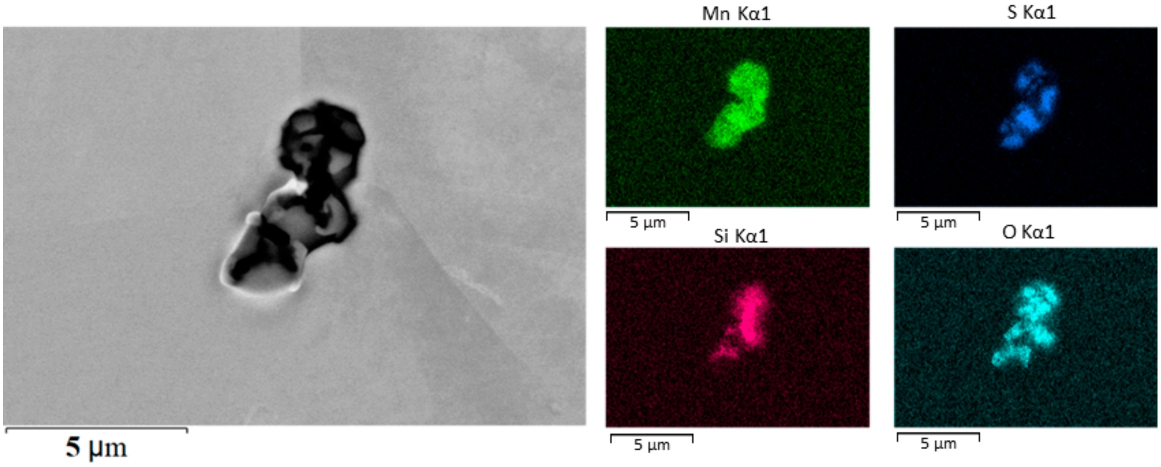

Figure 4. SEM image of manganese sulfide and silicon oxide inclusions in steel without additional alloying and the elemental mapping of Mn, S, Si, and O.

In the niobium-alloyed steel, manganese sulfide inclusions and niobium carbonitride precipitates were present. Figure 5 shows niobium inclusions arranged along the grain boundaries of the delta ferrite. EDS analysis showed the correlation of sulfur and manganese distribution and the correlation of areas enriched in chromium and depleted in nickel. Table 13 shows the point EDS analysis of the niobium precipitate shown in Figure 6.

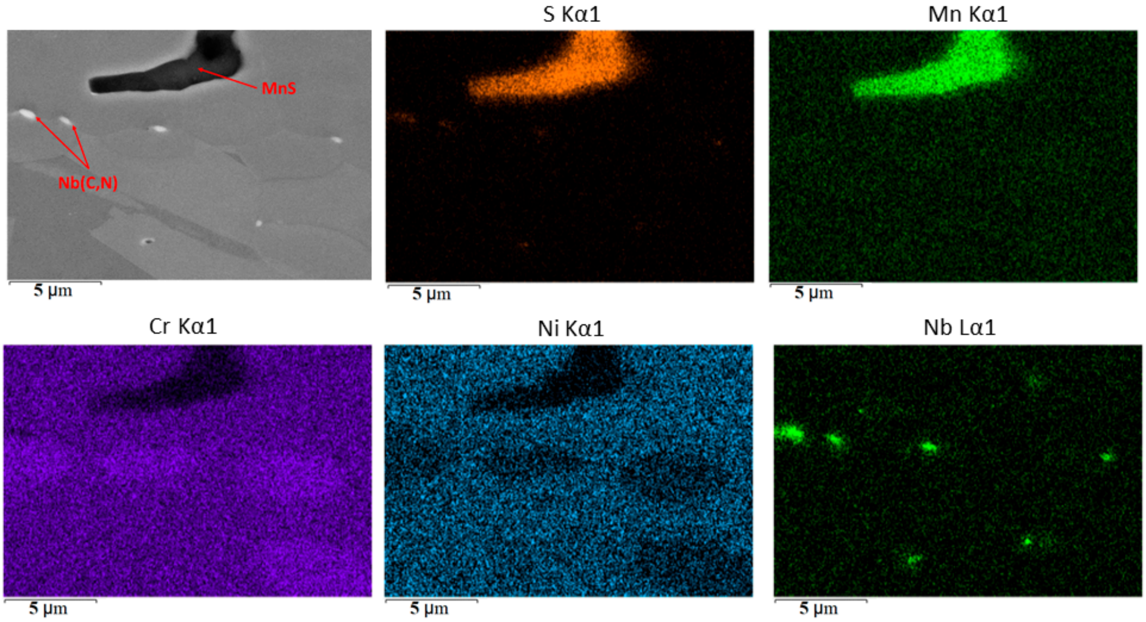

Figure 5. SEM image of manganese sulfide and niobium carbonitride inclusions in niobium-alloyed steel and the distribution of Mn, S, N, Cr, and Ni elements in the steel microstructure.

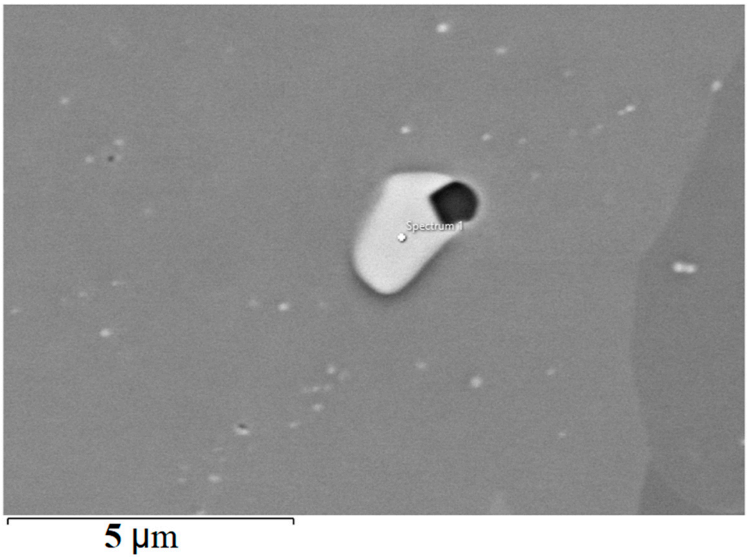

Figure 6. SEM image and location of point EDS analysis of a niobium carbonitride precipitate.

Table 13. Point EDS analysis of the niobium carbonitride precipitate (in wt.%) from Figure 6.

	C	N	Cr	Fe	Nb
Spectrum 1	34.14	2.93	0.38	0.74	61.81

In the titanium-alloyed steel, primarily titanium oxides were present due to the high content of dissolved oxygen. An example of this is shown in Figure 7, where we can see the correlation of Ti and O distribution in the EDS elemental mapping.

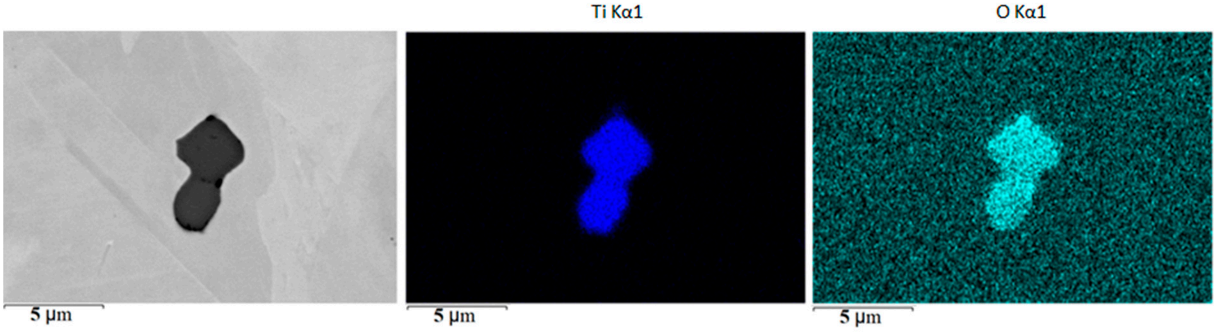

Figure 7. SEM image of a titanium oxide inclusion and the EDS elemental distribution mapping of Ti and O.

In the yttrium-alloyed steel, yttrium silicate was formed, which is confirmed by the simulation performed with ThermoCalc, and manganese sulfide and aluminum oxide also grew on the particles. An example of such a complex inclusion is shown in Figure 8. The EDS distribution of chemical elements in the steel microstructure shows a correlation of yttrium, silicon, aluminum, and oxygen, as well as a correlation of manganese and sulfur. Figure 9 shows point EDS analysis of yttrium oxide inclusions on grain boundary.

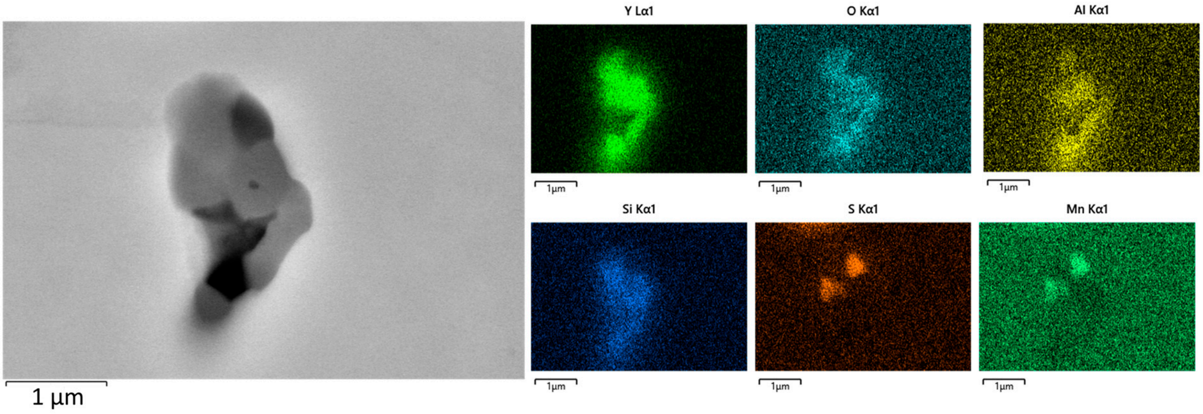

Figure 8. SEM image of a complex inclusion of yttrium silicate, manganese sulfide, and aluminum oxide and the EDS elemental distribution mapping of yttrium, oxygen, silicon, aluminum, manganese, and sulfur.

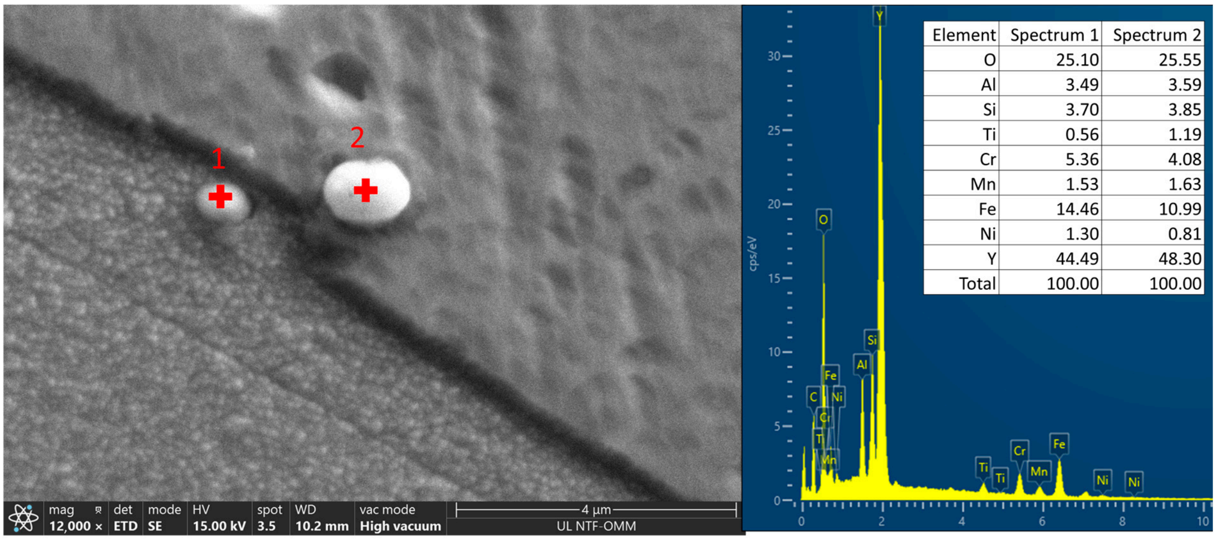

Element	Spectrum 1	Spectrum 2
O	25.10	25.55
Al	3.49	3.59
Si	3.70	3.85
Ti	0.56	1.19
Cr	5.36	4.08
Mn	1.53	1.63
Fe	14.46	10.99
Ni	1.30	0.81
Y	44.49	48.30
Total	100.00	100.00

Figure 9. SEM image of yttrium oxides on a grain boundary with elemental analysis.

In the zirconium-alloyed sample, there were primarily zirconium oxide particles on which manganese sulfide grew. Figure 10 shows the EDS analysis, which indicates a correlation of zirconium and oxygen and a correlation of manganese and sulfur. In addition, Figure 10 shows how the grain boundary was bowed where it was in contact with the inclusion, which demonstrates the mechanism of grain boundary pinning. This retards the movement of grain boundaries and slows down grain growth.

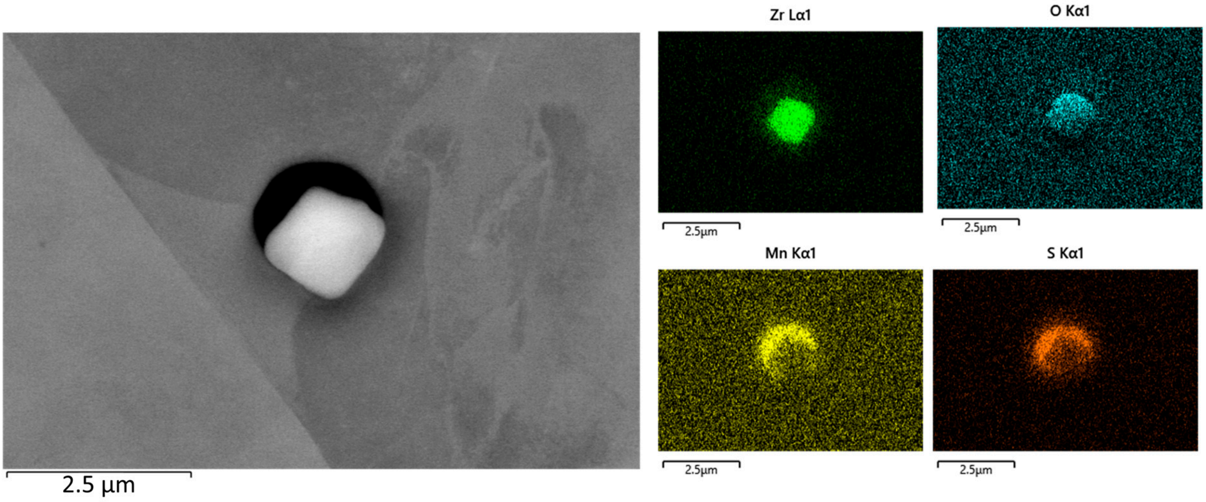

Figure 10. SEM image of a zirconium oxide and manganese sulfide inclusion and the EDS elemental distribution mapping of zirconium, oxygen, manganese, and sulfur.

3.4. Crystal Grain Size

Crystal grain sizes were measured using the comparison method defined by the ASTM E112 standard. The average grain diameter was determined for each sample. If a sample had a bimodal grain size distribution, the mean value was calculated and used as the average crystal grain size. An example of a bimodal grain size distribution is shown in Figure 11. Their sizes are listed in Tables 14 and 15. An example of a coarse crystal grain is shown in Figure 12.

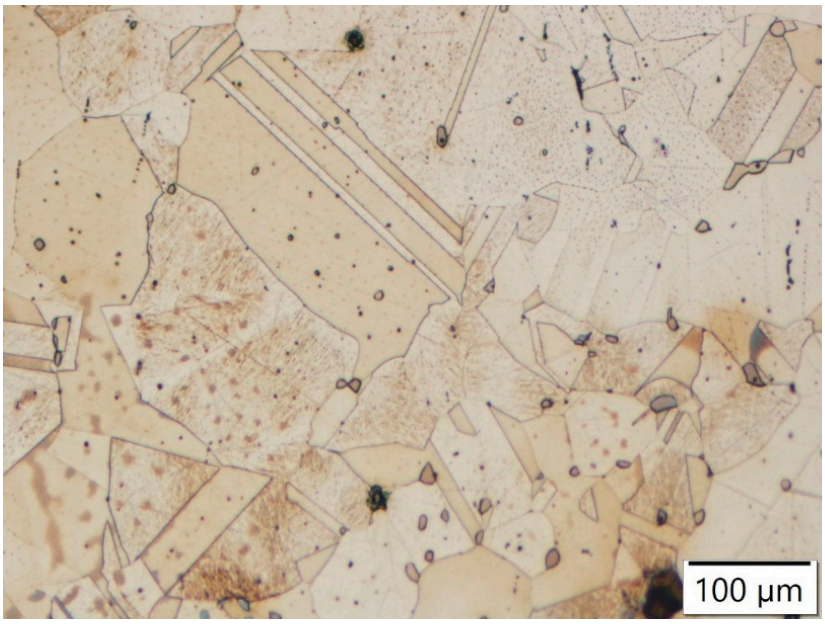

Figure 11. Example of a bimodal crystal grain size distribution.

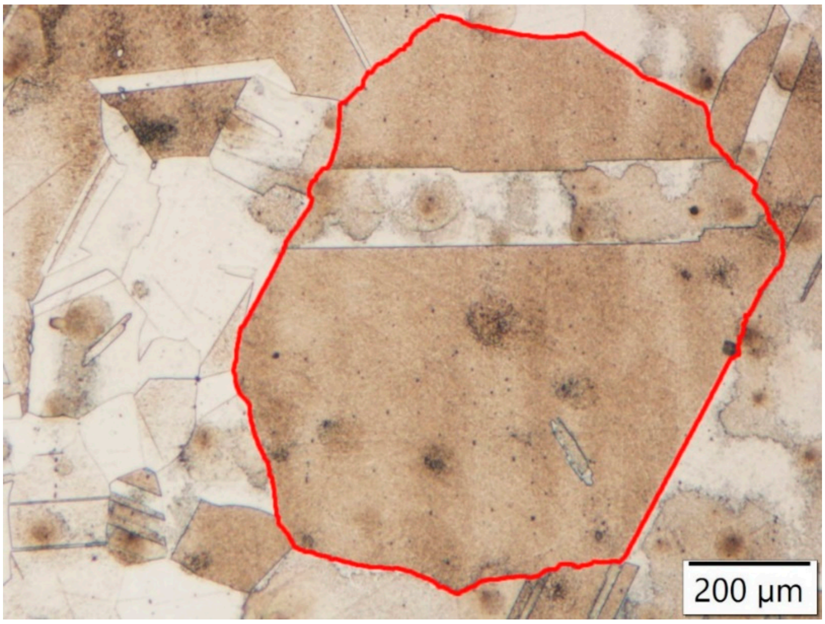

Figure 12. An exceptionally large austenitic crystal grain with a twin (grain boundary outlined with red).

Table 14. Average crystal grain sizes at annealing temperatures of 1050 °C and 1100 °C, measured according to the ASTM E112 standard.

	Temperature 1050 °C							**Temperature 1100 °C**					
	Annealing Time (h)							**Annealing Time (h)**					
	0	**0.5**	**1**	**2**	**4**	**8**		**0**	**0.5**	**1**	**2**	**4**	**8**
304-0	5.5	5	5	4	3.5	1.5	304-0	6.5	5.5	5	4.0	3.0	1.75
304-Nb	6	5.5	4.5	4.25	3.25	2.5	304-Nb	6	4.75	4	3.25	2.25	1.75
304-Ti	6.5	6.5	6.5	6.5	6.5	6	304-Ti	6.5	6.0	6.0	5.75	5.75	4.0
304-Y	6.25	6	5.5	4.5	3.0	2.0	304-Y	6	5.5	5.5	4	2.25	0.25
304-Zr	6	6	5.25	5.25	4.5	4.0	304-Zr	6.5	6.5	5	4.5	4	3.25

Table 15. Average crystal grain sizes at annealing temperatures of 1150 °C and 1200 °C, measured according to the ASTM E112 standard.

	Temperature 1150 °C							**Temperature 1200 °C**					
	Annealing Time (h)							**Annealing Time (h)**					
	0	**0.5**	**1**	**2**	**4**	**8**		**0**	**0.5**	**1**	**2**	**4**	**8**
304-0	6.5	5.5	2.25	2.0	1.0	0.25	304-0	4	2.0	1.75	1.25	0.25	0 [2]
304-Nb	6.0	5.0	4.0	3.5	1.5	0.5	304-Nb	4.5	4.25	3.75	1	0.5 [1]	0 [2]
304-Ti	5.5	5.0	5.0	4.0	2.0	1.25	304-Ti	6	5.5	4.75	1.5	0.25	0 [2]
304-Y	5.0	4.5	2.5	1.5	0.5	0.25	304-Y	6.5	5.5	3.75	3.25	2.5	0.75 [1]
304-Zr	6.25	5.5	5.0	4.25	4.0	2.0	304-Zr	6.5	2.0	2.0	1.75	0[2]	0 [2]

[1] Largest crystal grains, greater than 800 μm. [2] Largest crystal grains, greater than 1000 μm.

The reference steel (composition 304-0) showed significant grain growth at all annealing temperatures: at 1050 °C, the crystal grains grew from an initial size of 53 μm to a final size of 214 μm after eight hours. At 1100 °C, the grains grew from an initial size of 38 μm to a final size of 197 μm. At 1150 °C, they grew from an initial size of 38 μm to a final size of 330.5 μm, and at 1200 °C, they grew from an initial size of 90 μm to 359 μm. There were no microalloying element precipitates in this steel composition, so grain growth was practically uninhibited.

Niobium slightly inhibited grain growth at the lowest annealing temperature (1050 °C), with grains growing from an initial size of 45 µm to a size of 151 µm. It did not inhibit grain growth at higher temperatures. Titanium had the greatest effect on crystal grain size at annealing temperatures of 1050 °C and 1100 °C. The initial grain size at 1050 °C was 38 µm, and after eight hours, it was 45 µm. At 1100 °C, the initial crystal grain size was 38 µm, and the final size was 90 µm, which is significantly smaller than the grains of the reference steel. At 1150 °C, titanium was still effective at inhibiting grain growth up to two hours (the size was 90 µm), but at longer annealing times, the grains began to grow rapidly. At 1200 °C, the crystal grains became coarse after just one hour, and after eight hours, they were 359 µm—comparable to the grain size of the reference steel.

Yttrium had no effect on the crystal grain size up to an annealing temperature of 1200 °C. However, when annealed at 1200 °C, the yttrium-alloyed steel had the smallest crystal grains of all compositions. The initial crystal grain size was 38 µm, and after eight hours, it was 278 µm, which is relatively small compared to the reference steel (which grew from an initial size of 90 µm to 359 µm at the same temperature over eight hours). The reason for this is that the yttrium inclusions formed in the melt. Because of this, they were randomly distributed throughout the microstructure, and the crystal grains had to grow enough to come into contact with them. Niobium had a moderate influence on the crystal grain size only at the lowest annealing temperature (final crystal grain size was 151 µm), but it did not affect grain growth at higher temperatures.

The presence of microalloying element precipitates and inclusions was verified with a scanning electron microscope. Figure 13 shows an SEM image of titanium precipitates that inhibit grain growth. The grain boundary between the two precipitates is bowed in the direction of grain growth.

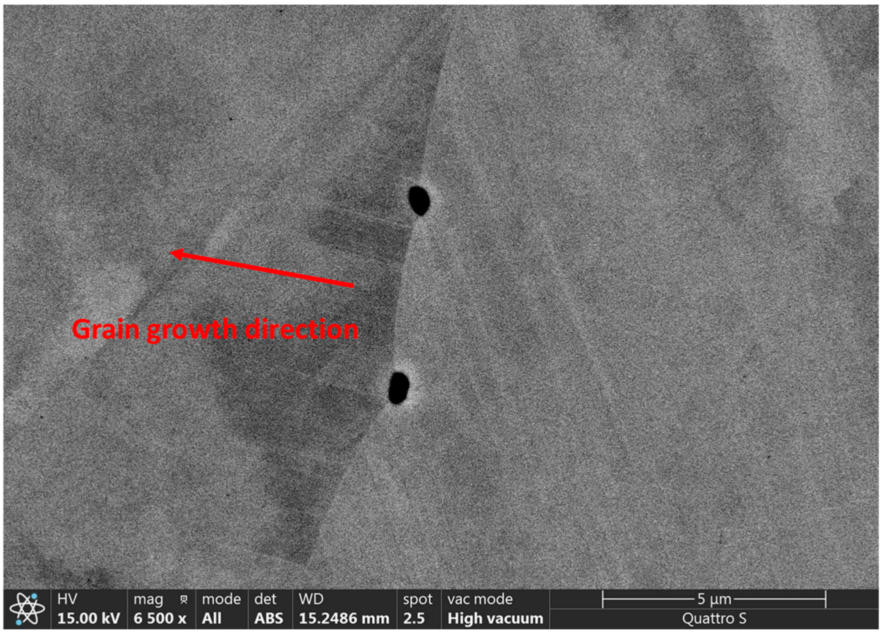

Figure 13. SEM image of Ti(C,N) precipitates on a grain boundary with the direction of grain growth indicated.

The grain growth at different annealing temperatures up to eight hours is summarized in Figures 14–17.

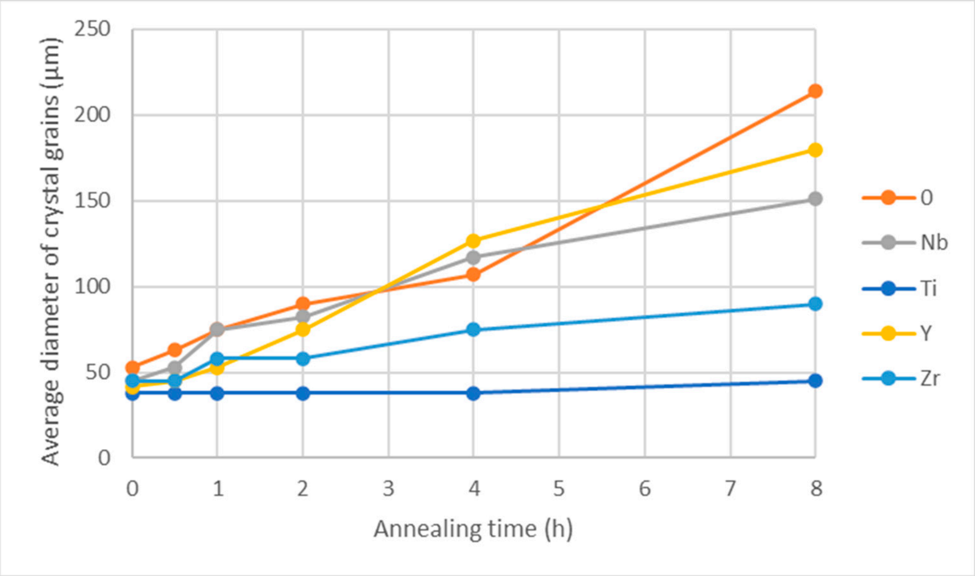

Figure 14. Crystal grain size as a function of annealing time at 1050 °C.

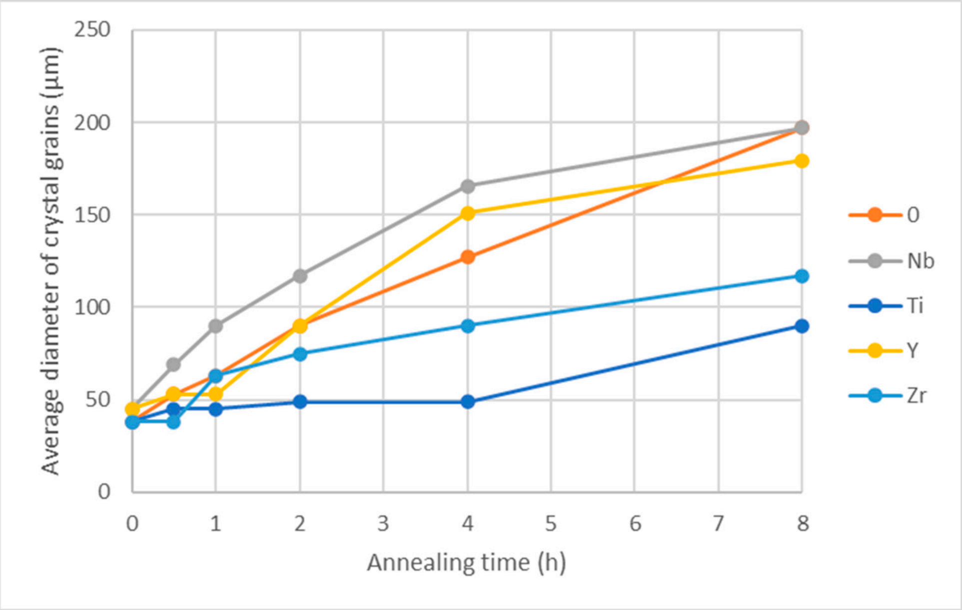

Figure 15. Crystal grain size as a function of annealing time at 1100 °C.

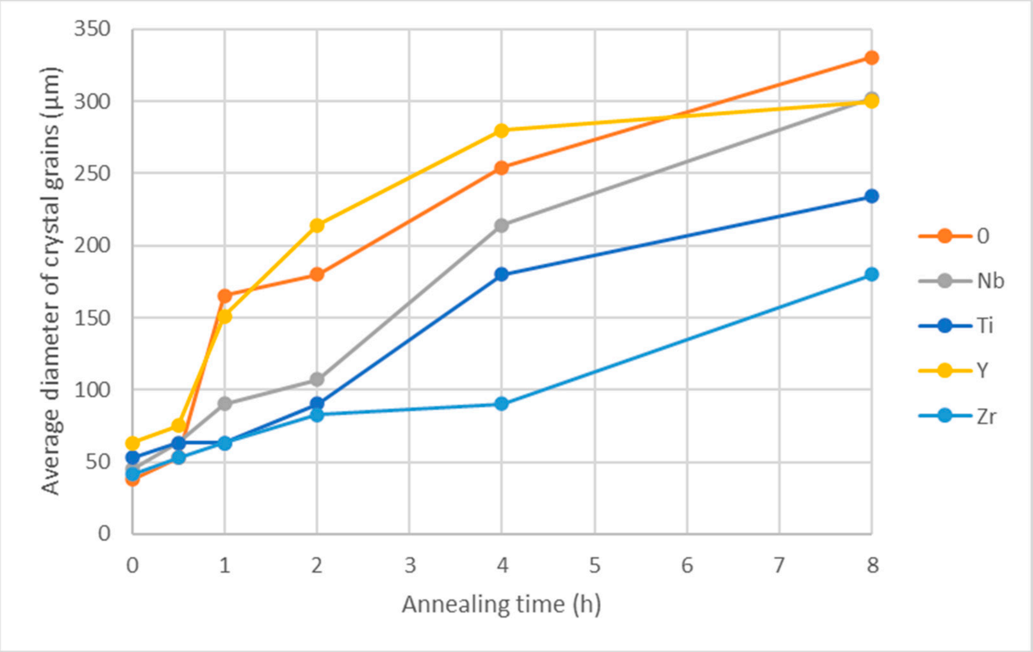

Figure 16. Crystal grain size as a function of annealing time at 1150 °C.

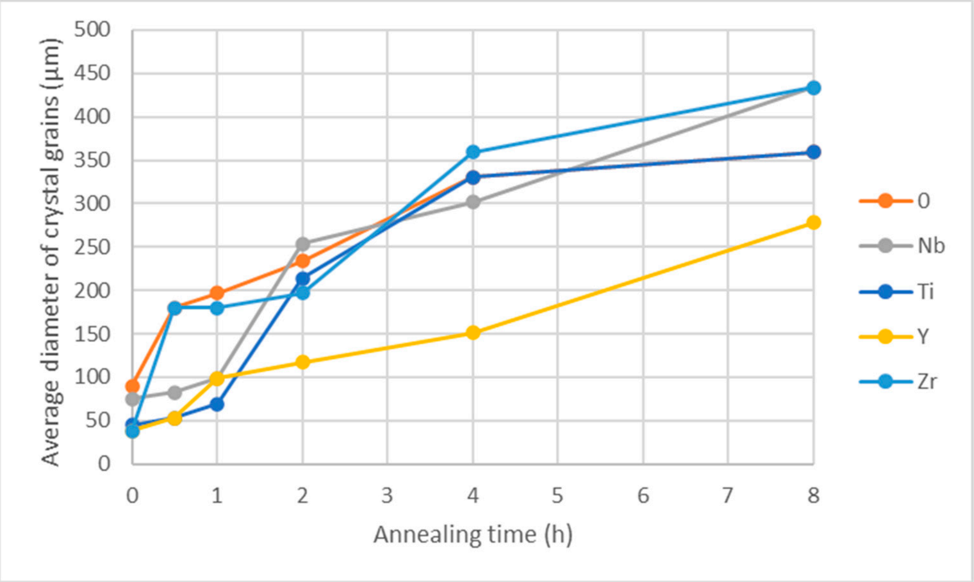

Figure 17. Crystal grain size as a function of annealing time at 1200 °C.

As can be seen from Figure 18, the microstructure of the Ti-alloyed steel (45 µm) is finer after eight hours of annealing at 1050 °C than all other samples (Figure 18a). We can also see that the reference steel (218 µm, Figure 18b) and the Y-alloyed steel (180 µm, Figure 18c) experienced substantial grain growth after eight hours of annealing at 1050 °C. The Zr microalloying addition was somewhat more effective at inhibiting grain growth; the grain size was 90 µm after 8 h at 1050 °C (Figure 18d).

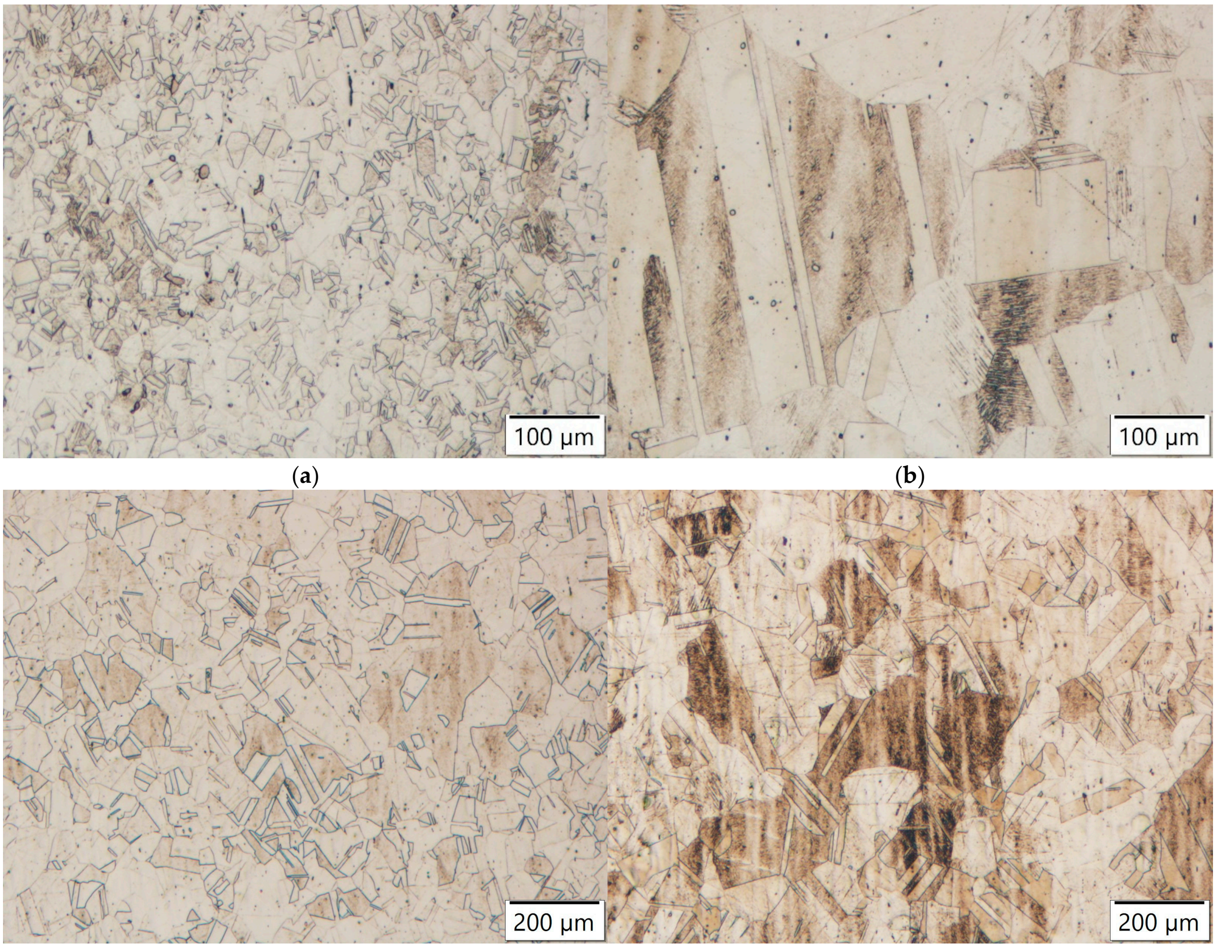

(**a**) (**b**)

(**c**) (**d**)

Figure 18. Microstructures of steel samples annealed at 1050 °C for 8 h: (**a**) Ti-alloyed steel; (**b**) reference steel; (**c**) Zr-alloyed steel (**d**) Y-alloyed steel.

As can be seen from Figure 19, the Ti-alloyed steel experienced almost no grain growth up to 4 h of annealing at 1100 °C (49 µm, Figure 19a). The Nb-alloyed steel (166 µm) had substantial grain growth after 4 h of annealing at 1100 °C (Figure 19b). Zr was still less effective than Ti, as the Zr-alloyed sample had 90 µm crystal grains after 4 h at 1100 °C (Figure 19c), while Y did not show any significant grain size retention after 4 h at 1100 °C (151 µm, Figure 19d).

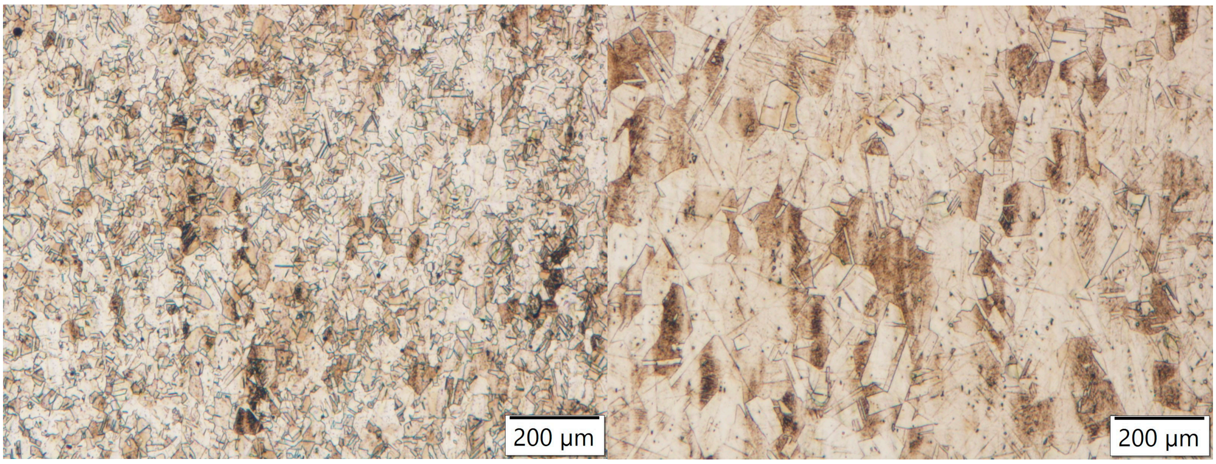

(**a**) (**b**)

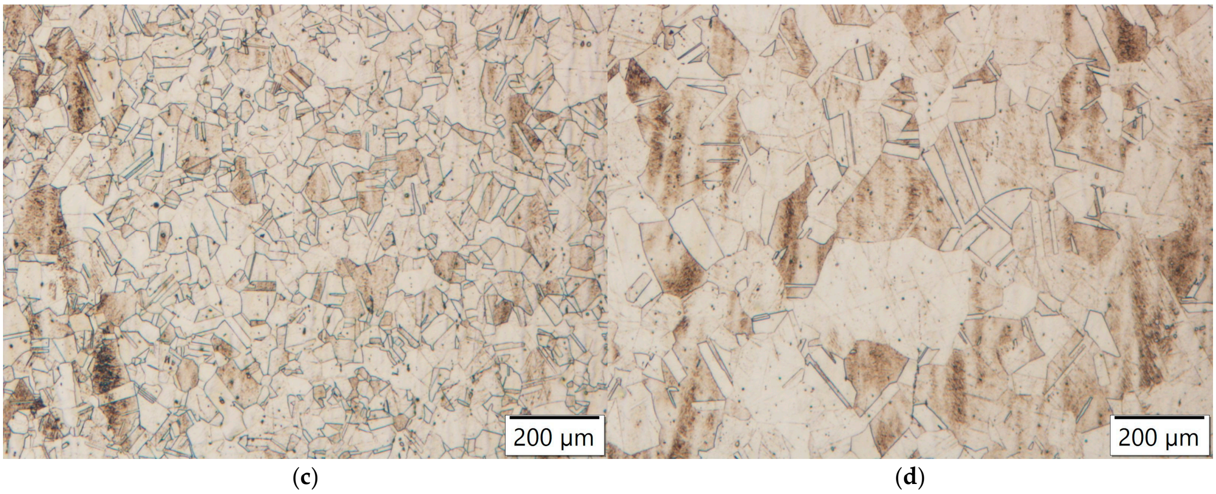

(**c**) (**d**)

Figure 19. Microstructures of steel samples annealed at 1100 °C for 4 h: (**a**) Ti-alloyed steel; (**b**) Nb-alloyed steel; (**c**) Zr-alloyed steel; (**d**) Y-alloyed steel.

As can be seen from Figure 20, there is a significant difference in the grain sizes after four hours of annealing at 1150 °C. The Zr-alloyed steel effectively inhibited grain growth up to four hours of annealing at 1150 °C (90 µm, Figure 20a). The reference steel again exhibited coarse grains (254 µm, Figure 20b) after four hours of annealing at 1150 °C, The Nb-alloyed steel also exhibited coarse grain size (214 µm, Figure 20c). The Ti-alloyed steel samples exhibited a bit finer grains (180 µm, Figure 20d).

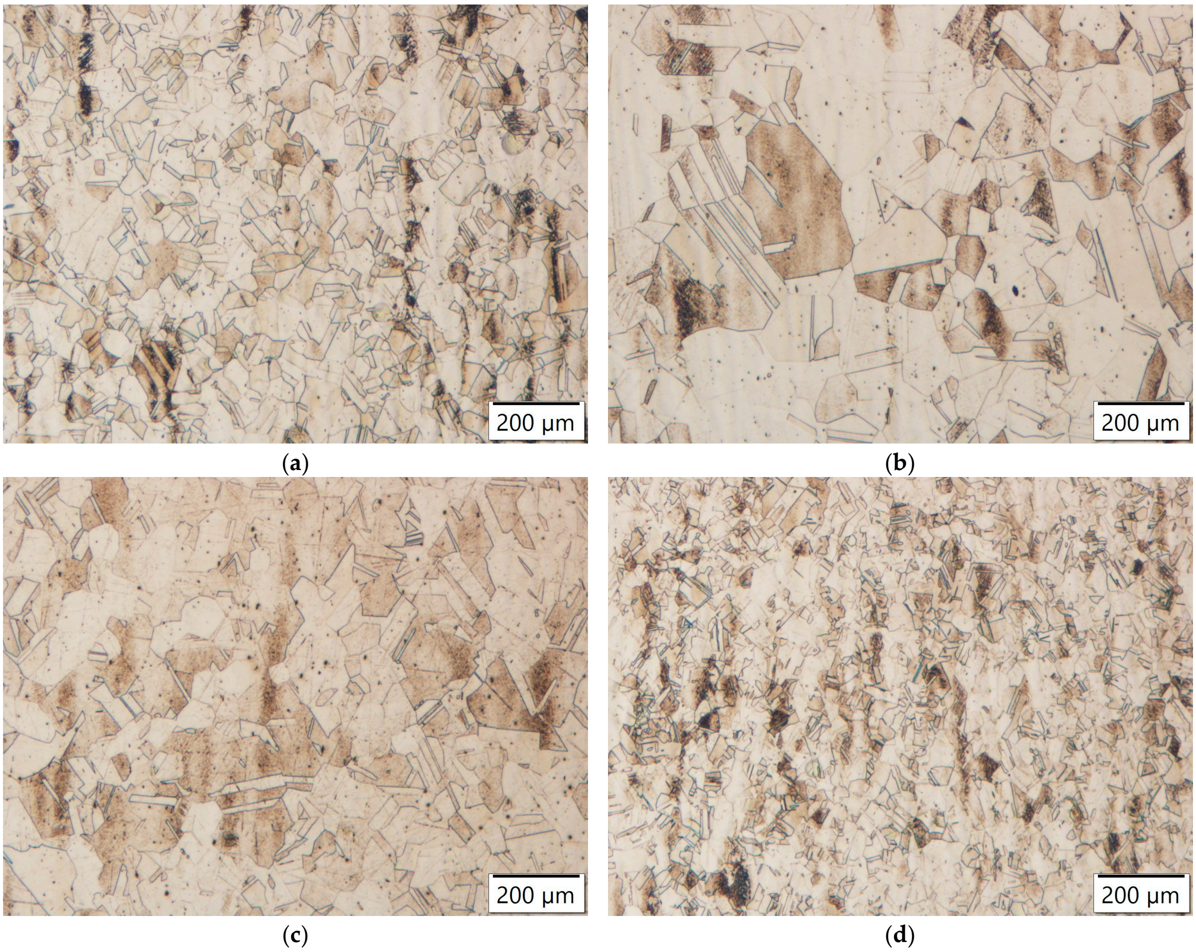

(**a**) (**b**) (**c**) (**d**)

Figure 20. Microstructures of samples annealed at 1150 °C for 4 h: (**a**) Zr-alloyed steel; (**b**) reference steel; (**c**) Nb-alloyed steel; (**d**) Ti-alloyed steel.

As can be seen from Figure 21 the crystal grains coarsened at 1200 °C after four hours of annealing. All the steel samples exhibit very coarse grains the average size was above 300 μm, Zr-alloyed steel 359 μm (Figure 21a), Ti alloyed steel 330 μm (Figure 21b), and the reference steel sample also 330 μm (Figure 21c), except for the Y-alloyed steel sample, where the average grain size was 151 μm (Figure 21d). But even the Y-alloyed steel samples experienced significant growth when annealed for eight hours.

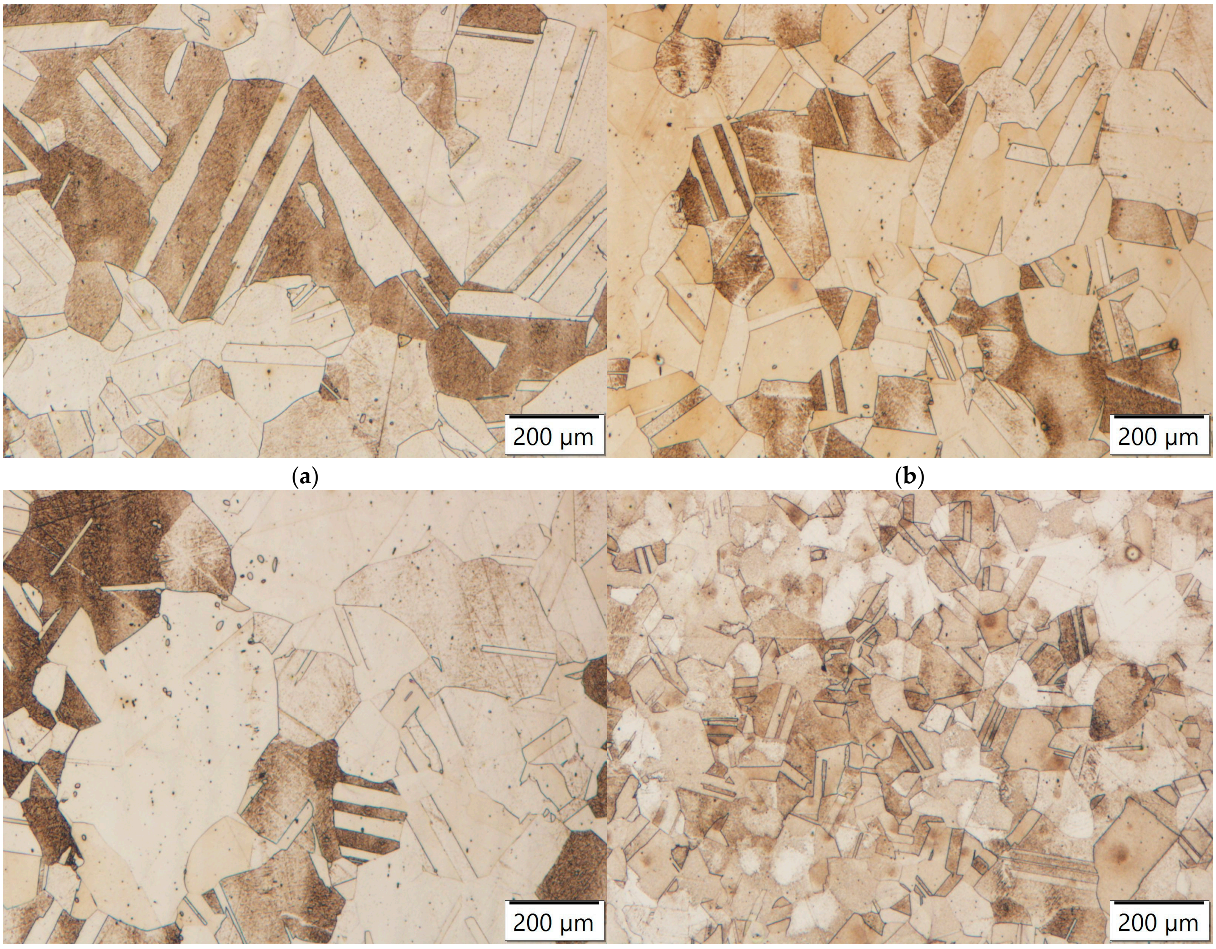

(**a**) (**b**)

(**c**) (**d**)

Figure 21. Microstructures of samples annealed at 1150 °C for 4 h: (**a**) Zr-alloyed steel, (**b**) Ti-alloyed steel; (**c**) reference steel; (**d**) Y-alloyed steel.

The Y-alloyed samples only showed pinning at 1200 °C, where the grain sizes were the largest. This means that the Y-rich particles were sparsely located and did not show any pinning effect due to the relatively large distances between them. Yttrium additions are known to inhibit grain growth [44,45].

3.5. Crystal Grain Growth Model

The crystal grain growth model was developed based on the modified Sellars-Whiteman model [9]. We used it due to the good agreement between the calculated and measured values. Equation (1) shows the adapted crystal grain growth model:

$$D = D_0 + K \times t^{\frac{n}{T}} \times e^{\left(\frac{-Q}{RT}\right)} \quad (1)$$

where D is the average crystal grain size, D_0 is the average crystal grain size at time 0, K and n are constants, t is time, and T is temperature. First, we took the logarithm of the equation, which gave us Equation (2):

$$\ln(\mathrm{D}-\mathrm{D}_0)=\ln(\mathrm{k})+\frac{\mathrm{n}}{\mathrm{T}}\times\ln(\mathrm{t})-\frac{\mathrm{Q}}{\mathrm{RT}} \quad (2)$$

Since the relationship between $\ln(D - D_0)$ and $\ln(t)$ is linear, linear regression gives us an initial value of n, which is 0.943, so n = 1247. The relationship between $\ln(D - D_0)$ and 1/T is also linear, so linear regression gives us Q/R, which is 20,013.24, meaning Q is 166,390 J/mol. The initial value of k was obtained by substituting the experimental values for n and Q into Equation (1). For better agreement between the model and the measured values, the values of n and k were then adjusted. The model showed the best agreement when the value of n was 1247 for temperatures of 1050 and 1100 °C, while n = 930 was more appropriate for temperatures of 1150 and 1200 °C. The values of k also changed with temperature: at 1050 °C it was 1.8×10^6, at 1100 °C 1.3×10^6, at 1150 °C 8.0×10^6, and at 1200 °C 6.1×10^6. Figure 22 shows comparisons of the calculated and measured values for crystal grain sizes. As can be seen, the model agrees well with the measured values up to four hours, but deviations occur at longer annealing times. This is not a problem, as austenitic stainless steels are rarely annealed for such long times in industry.

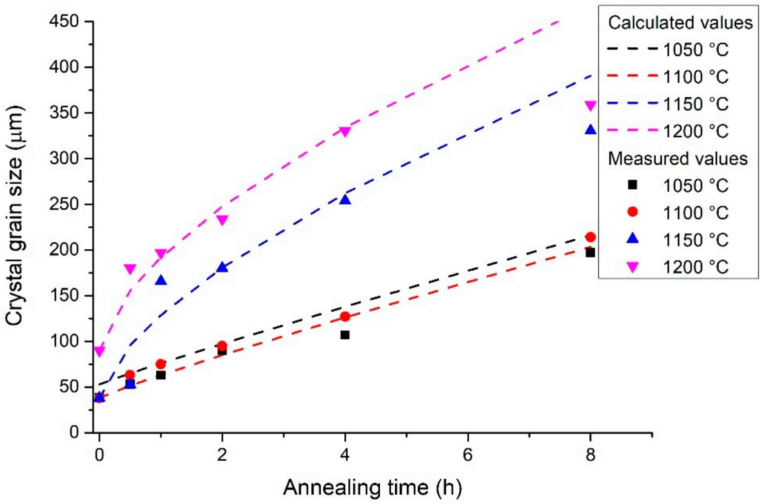

Figure 22. Comparison of experimentally measured austenitic crystal grain size with calculated values as a function of temperature and time, in steel without microalloying elements.

3.6. Brinell Hardness

Figures 23–26 show the results of the hardness measurements. A general trend of decreasing hardness with increasing annealing time is observed for all samples. At an annealing temperature of 1050 °C, the niobium-alloyed steel was significantly harder than the others (after eight hours of annealing, it had a hardness of 156.27 HB compared to the reference steel, which had the second-highest value with a hardness of 136.38 HB). This can be attributed to precipitation hardening by Nb(C,N). At 1100 °C, the titanium-alloyed steel had the highest hardness (hardness after eight hours of annealing was 150.29 HB, compared to the Nb-alloyed steel which had a hardness of 136.6 HB). At 1150 °C, the difference in hardness between the Ti-alloyed steel (147 HB) and the other compositions (between 127 and 141 HB) decreased at longer annealing times. At 1200 °C, the hardness values of all compositions were comparable (between 130 and 138 HB).

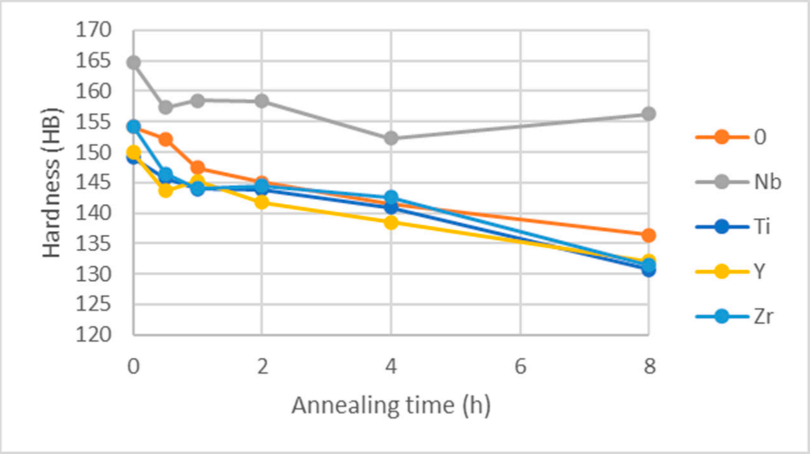

Figure 23. Brinell hardness for samples annealed at 1050 °C.

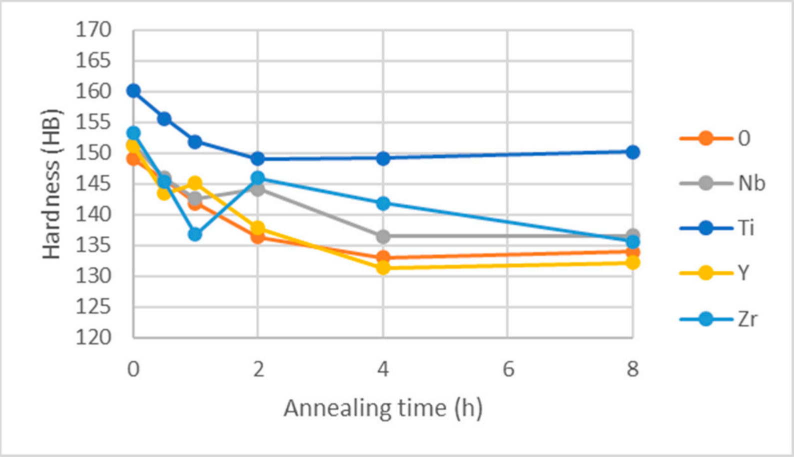

Figure 24. Brinell hardness for samples annealed at 1100 °C.

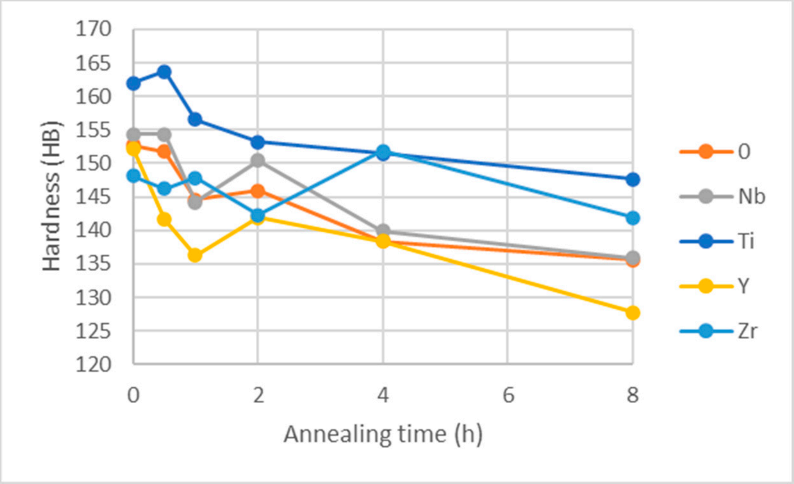

Figure 25. Brinell hardness for samples annealed at 1150 °C.

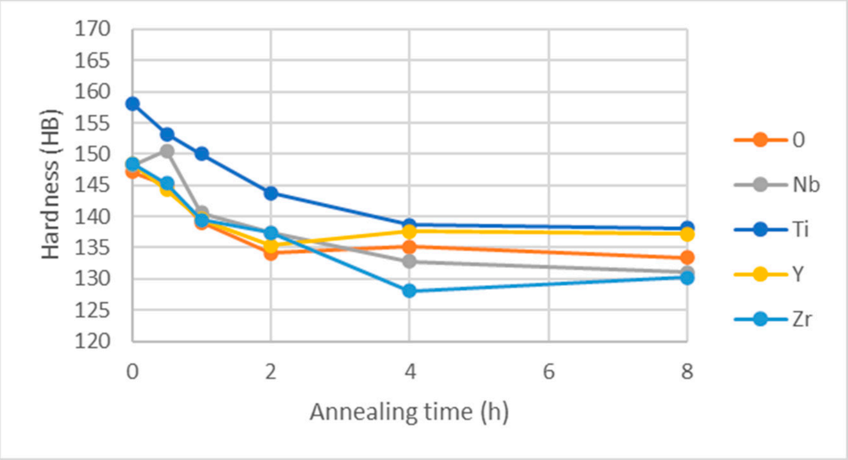

Figure 26. Brinell hardness for samples annealed at 1200 °C.

3.7. ThermoCalc Simulation

We performed a stable phase simulation in the ThermoCalc program. Figure 27 shows the phase fractions as a function of temperature. FCC_A1 is austenite, which serves as the metallic matrix, BCC_A2 is ferrite, which forms at high temperatures as delta-ferrite and at low temperatures as alpha-ferrite. LIQUID is the melt, M23C6 is chromium carbide, most typical in unstabilized steels. SIGMA represents the sigma phase, which is an intermetallic compound of iron and chromium.

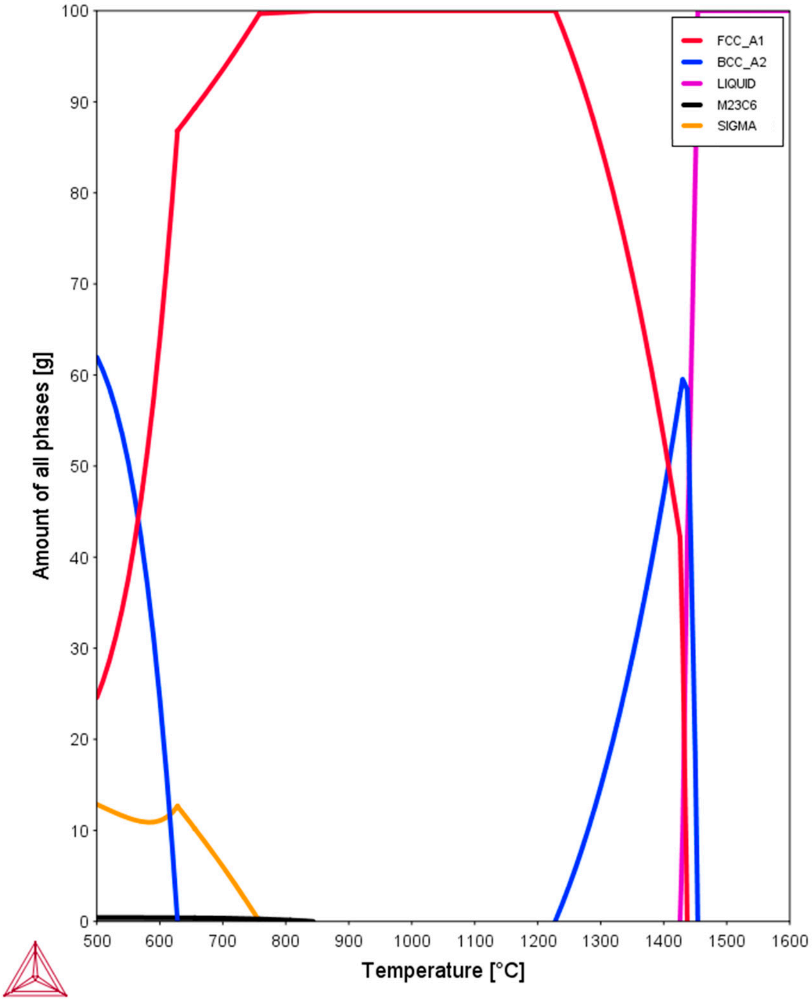

Figure 27. Simulation of stable phases for steel without microalloying elements.

Figure 28 shows the phases of precipitates and inclusions that inhibit grain growth. Niobium carbonitrides completely dissolve between temperatures of 1050 and 1100 °C, which corresponds to the obtained results. The solubility of titanium nitride decreases rapidly with increasing temperature, although it is present up to the melting temperature. Zirconium nitride has a relatively constant fraction up to the melting temperature. The ThermoCalc program calculated that yttrium forms a silicate, but we believe that only an oxide was formed. We confirmed our suspicion with a chemical analysis of the inclusions using an energy-dispersive X-ray spectrometer (EDS). Yttrium oxide forms in the melt, so it is present at all annealing temperatures.

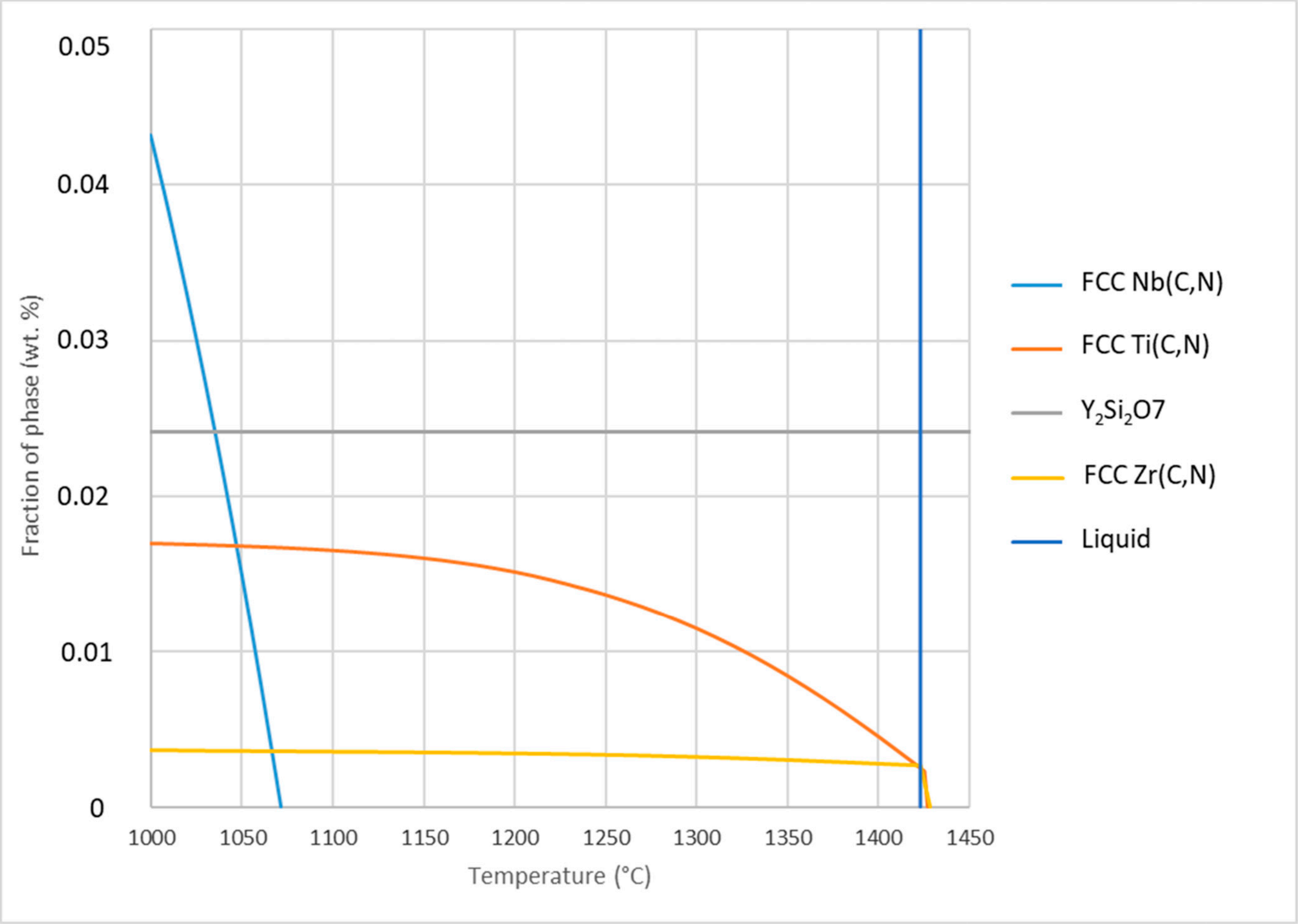

Figure 28. Fraction of stable phases as a function of temperature, calculated with ThermoCalc.

4. Conclusions

We investigated the effect of microalloying elements niobium, titanium, yttrium, and zirconium on the growth of austenitic crystal grains in AISI 304 stainless steel at annealing temperatures from 1050 to 1200 °C and annealing times from zero to eight hours. The most important findings can be summarized in the following conclusions:

- In steel without microalloying elements, the crystal grains grew from 53 µm to 197 µm at 1050 °C or to 359 µm at 1200 °C. The microstructure consisted of austenite with a small amount of delta-ferrite and inclusions of MnS and SiO_2. In the Nb-alloyed steel, Nb(C,N) was also present in the microstructure; in the Ti-alloyed steel, Ti(C,N) and titanium oxide inclusions were present; in the Zr-alloyed steel, zirconium oxide inclusions were present; and in the Y-alloyed steel, yttrium oxide inclusions were present.

- The amount of delta-ferrite in the as-cast state was around 10 vol.%, and in the as-rolled state, it was around 7 vol.%. In the steel heated to the highest annealing temperature of 1200 °C, there was only about 1.4 vol.% of delta-ferrite, and after eight hours of annealing, its content was below the detection limit of the feritometer. The delta-ferrite content decreased to a value between 0.5 and 1.5 vol.% after one hour of annealing at 1100 °C and 1150 °C. At 1050 °C, due to the lower temperature, the delta-ferrite content only reached these values after two hours of annealing. The annealing temperature has a greater influence on the delta-ferrite content at shorter annealing times than at longer ones.
- Titanium had the greatest effect on inhibiting crystal grain growth by pinning grain boundaries, but only up to an annealing temperature of 1100 °C. The effect of zirconium was slightly less, but it was more effective than titanium at higher temperatures (up to 1150 °C). At the highest annealing temperature (1200 °C), only yttrium influenced the slowing of crystal grain growth. Niobium had an effect only at the lowest annealing temperature (1050 °C), where it slightly inhibited crystal grain growth. To describe the growth of austenitic crystal grains in AISI 304 steel, we developed a model based on the Arrhenius-type Sellars–Whiteman equation, which shows good agreement between the measured and calculated values up to an annealing time of four hours.
- After annealing at the lowest temperature (1050 °C), the niobium-alloyed steel had the highest hardness (between 156 and 165 HB), even though it did not have the smallest crystal grains. We attribute this to precipitation hardening with Nb(C,N). After annealing at the other temperatures, the titanium-alloyed steel was the hardest (between 138 and 150 HB).

Author Contributions: Conceptualization, J.B. and A.N.; methodology, J.B.; software, J.B.; validation, J.B., S.T. and A.N.; formal analysis, A.N.; investigation, S.T. and A.N.; writing—original draft preparation, J.B. and S.T.; writing—review and editing, J.B. and A.N.; visualization, S.T.; supervision, J.B. and A.N. All authors have read and agreed to the published version of the manuscript.

Funding: This research was funded by ARIS, grant number P2-0050.

Data Availability Statement: The data presented in this study are available on request from the corresponding author. The data is not available due to privacy.

Conflicts of Interest: The authors declare no conflicts of interest.

References

1. Liu, M.; Gong, W.; Zheng, R.; Li, J.; Zhang, Z.; Gao, S.; Ma, C.; Tsuji, N. Achieving Excellent Mechanical Properties in Type 316 Stainless Steel by Tailoring Grain Size in Homogeneously Recovered or Recrystallized Nanostructures. *Acta Mater.* **2022**, *226*, 117629. https://doi.org/10.1016/j.actamat.2022.117629.
2. Shirdel, M.; Mirzadeh, H.; Habibi Parsa, M. Microstructural Evolution during Normal/Abnormal Grain Growth in Austenitic Stainless Steel. *Met. Mater. Trans. A* **2014**, *45*, 5185–5193. https://doi.org/10.1007/s11661-014-2426-7.
3. Lan, P.; Liu, H.; Zhang, L.; Lu, Y.; Zhang, J.; Chen, L.; Wen, R.; Wang, P. Austenite Grain Growth Kinetics in Continuously Cast Low Alloyed Steels at High Temperature. *Metall. Mater. Trans. B* **2025**, *56*, 170–185. https://doi.org/10.1007/s11663-024-03347-0.
4. Bajželj, A.; Burja, J. Influence of Austenitisation Time and Temperature on Grain Size and Martensite Start of 51CrV4 Spring Steel. *Crystals* **2022**, *12*, 170–185. https://doi.org/10.3390/cryst12101449.
5. Wang, Y.; Wang, H.; Peng, S.; Xia, B.; Zhu, H. The Dominant Role of Recrystallization and Grain Growth Behaviors in the Simulated Welding Heat-Affected Zone of High-Mn Steel. *Materials* **2024**, *17*, 2218. https://doi.org/10.3390/ma17102218.
6. Sun, X.; Gao, S.; Shang, W.; Zhong, Q.; Song, G.; Zhao, S. Effects of Ti and N Contents on the Characteristic Evolution and Thermal Stability of MC Carbonitrides Holding at 1250 °C in H13 Die Steel. *Metals* **2024**, *14*, 317. https://doi.org/10.3390/met14030317.

7. Napoli, G.; Di Schino, A. Modelling Grain Growth Kinetics in Steels. *Arch. Metall. Mater.* **2018**, *63*, 839–844. https://doi.org/10.24425/122412.
8. Rios, P.R.; Zöllner, D. Grain Growth–Unresolved Issues. *Mater. Sci. Technol.* **2018**, *34*, 629–638. https://doi.org/10.1080/02670836.2018.1434863.
9. Sellars, C.M.; Whiteman, J.A. Recrystallization and Grain Growth in Hot Rolling. *Met. Sci.* **1979**, *13*, 187–194. https://doi.org/10.1179/msc.1979.13.3-4.187.
10. Fredriksson, H. Mechanism of Grain Growth in Metals. *Mater. Sci. Technol.* **1990**, *6*, 811–818. https://doi.org/10.1179/mst.1990.6.9.811.
11. Fujiyama, N.; Nishibata, T.; Seki, A.; Hirata, H.; Ogawa, K. Austenite Grain Growth Simulation Considering the Solute-Drag Effect and Pinning Effect. *Sci. Technol. Adv. Mater.* **2017**, *18*, 88–95. https://doi.org/10.1080/14686996.2016.1244473.
12. Farag, S.; Konyashin, I.; Ries, B. The Influence of Grain Growth Inhibitors on the Microstructure and Properties of Submicron, Ultrafine and Nano-Structured Hardmetals—A Review. *Int. J. Refract. Met. Hard Mater.* **2018**, *77*, 12–30.
13. Lee, S.J.; Lee, Y.K. Prediction of Austenite Grain Growth during Austenitization of Low Alloy Steels. *Mater. Des.* **2008**, *29*, 1840–1844. https://doi.org/10.1016/j.matdes.2008.03.009.
14. Sobotka, E.; Kreyca, J.; Fuchs, N.; Wojcik, T.; Kozeschnik, E.; Povoden-Karadeniz, E. The Role of MX Carbonitrides for the Particle-Stimulated Nucleation of Ferrite in Microalloyed Steel. *Met. Mater. Trans. A Phys. Met. Mater. Sci.* **2023**, *54*, 2903–2923. https://doi.org/10.1007/s11661-023-07067-z.
15. Tang, E.; Yuan, Q.; Zhang, R.; Zhang, Z.; Mo, J.; Liang, W.; Xu, G. On the Grain Coarsening Behavior of 20CrMnTi Gear Steel during Pseudo Carburizing: A Comparison of Nb-Ti-Mo versus Ti-Mo Microalloyed Steel. *Mater. Charact.* **2023**, *203*, 113138. https://doi.org/10.1016/j.matchar.2023.113138.
16. Wang, Y.; Zheng, Z.; Shi, R.; Zhang, B.; Zhou, X.; Pang, X.; Luo, W.; Wang, Z. Experimental Validation and Thermodynamics Analysis of (Nb, V)(C, N) Coupling Precipitation in High-Strength Spring Steel FAS3550. *Mater. Res. Express* **2023**, *10*, 054004. https://doi.org/10.1088/2053-1591/acd7c5.
17. Sawada, M.; Adachi, K.; Maeda, T. Effect of V, Nb and Ti Addition and Annealing Temperature on Microstructure and Tensile Properties of AISI 301L Stainless Steel. *ISIJ Int.* **2011**, *51*, 991–998.
18. Grabnar, K.; Burja, J.; Balaško, T.; Nagode, A.; Medved, J. The Influence of Nb, Ta and Ti Modification on Hot-Work Tool-Steel Grain Growth during Austenitization. *Mater. Tehnol.* **2022**, *56*, 331–338.
19. Foder, J.; Burja, J.; Klančnik, G. Grain Size Evolution and Mechanical Properties of Nb, v–Nb, and Ti–Nb Boron Type S1100ql Steels. *Metals* **2021**, *11*, 492. https://doi.org/10.3390/met11030492.
20. Bin Han, S.; Song, H.; Park, S.H. Improvement of Tensile Properties through Nb Addition and Heat Treatment in Additively Manufactured 316L Stainless Steel Using Directed Energy Deposition. *J. Mater. Res. Technol.* **2024**, *29*, 4806–4821. https://doi.org/10.1016/j.jmrt.2024.02.184.
21. Zhang, Y.; Li, X.; Liu, Y.; Liu, C.; Dong, J.; Yu, L.; Li, H. Study of the Kinetics of Austenite Grain Growth by Dynamic Ti-Rich and Nb-Rich Carbonitride Dissolution in HSLA Steel: In-Situ Observation and Modeling. *Mater. Charact.* **2020**, *169*, 110612. https://doi.org/10.1016/j.matchar.2020.110612.
22. Gong, S.; Su, L.; Wang, F. Nucleation and Coarsening Behavior of Aluminum Nitride and Its Effect on Abnormal Grain Growth in High-Temperature Carburizing Process. *Met. Mater. Trans. A* **2024**, *55*, 910–922. https://doi.org/10.1007/s11661-023-07294-4.
23. Li, L.; Ravikiran, K.; Sharma, N.K.; Choudhury, S.D.; Kannan, R.; Gaudet, M.J.; Anderson, N. Dissolution of Nb(C,N) During Post-Weld Heat-Treatment of Electric Resistance Welded X70 Line Pipe. *Met. Mater. Trans. A* **2024**, *55*, 3351–3363. https://doi.org/10.1007/s11661-024-07496-4.
24. Wang, N.; Wen, Y.; Chen, L.Q. Pinning of Grain Boundary Migration by a Coherent Particle. *Philos. Mag. Lett.* **2014**, *94*, 794–802. https://doi.org/10.1080/09500839.2014.978408.
25. Wang, N.; Ji, Y.; Wang, Y.; Wen, Y.; Chen, L.Q. Two Modes of Grain Boundary Pinning by Coherent Precipitates. *Acta Mater.* **2017**, *135*, 226–232. https://doi.org/10.1016/j.actamat.2017.06.031.
26. Peng, H.R.; Liu, W.; Hou, H.Y.; Liu, F. Pinning Effect of Coherent Particles on Moving Planar Grain Boundary: Theoretical Models and Molecular Dynamics Simulations. *Materialia* **2019**, *5*, 100225. https://doi.org/10.1016/j.mtla.2019.100225.
27. Fu, L.M.; Wang, H.R.; Wang, W.; Shan, A.D. Austenite Grain Growth Prediction Coupling with Drag and Pinning Effects in Low Carbon Nb Microalloyed Steels. *Mater. Sci. Technol.* **2011**, *27*, 996–1001. https://doi.org/10.1179/1743284711Y.0000000001.
28. Ye, L.; Wang, J.; Zeng, Z.; Wang, W.; Song, S.; Reddy, K.M.; Wang, L.; Wang, X. Realization of Selective Strengthening of Ferrite by Nb/V Microalloying in a Medium Carbon Lightweight δ-TRIP Steel. *Metall. Mater. Trans. A* **2020**, *51*, 2460–2468. https://doi.org/10.1007/s11661-020-05676-6.

29. Burja, J.; Nagode, A.; Medved, J.; Balaško, T.; Grabnar, K. Effect of Microalloying on Tempering of Mo-W High Thermal Conductivity Steel. *Metall. Ital.* **2023**, *114*, 22–27.
30. Qin, B.; Wang, Z.Y.; Sun, Q.S. Effect of Tempering Temperature on Properties of $00Cr_{16}Ni_5Mo$ Stainless Steel. *Mater. Charact.* **2008**, *59*, 1096–1100. https://doi.org/10.1016/j.matchar.2007.08.025.
31. Li, J.; Zhang, C.; Liu, Y. Influence of Carbides on the High-Temperature Tempered Martensite Embrittlement of Martensitic Heat-Resistant Steels. *Mater. Sci. Eng. A* **2016**, *670*, 256–263. https://doi.org/10.1016/j.msea.2016.06.025.
32. Cobb, H.M. *The History of Stainless Steel*; John Wiley & Sons: Hoboken, NJ, USA, 2011; Volume 48, ISBN 9781615030118.
33. Burja, J.; Lindič, J.; Šetina Batič, B.; Nagode, A. Temperature-Dependent Martensitic Transformation in Cold-Rolled AISI 304 Stainless Steel. *Crystals* **2025**, *15*, 652. https://doi.org/10.3390/cryst15070652.
34. Zhao, M.; Wu, H.; Lu, J.; Sun, G.; Du, L. Effect of Grain Size on Mechanical Property and Corrosion Behavior of a Metastable Austenitic Stainless Steel. *Mater. Charact.* **2022**, *194*, 112360. https://doi.org/10.1016/j.matchar.2022.112360.
35. Xu, Y.; Liu, J.; Zhao, Y.; Jiao, Y. Austenite Grain Growth Kinetics and Mechanism of Grain Growth in 12Cr Ultra-Super-Critical Rotor Steel. *Philos. Mag.* **2020**, *101*, 77–95. https://doi.org/10.1080/14786435.2020.1821113.
36. Baker, T.N. Microalloyed Steels. *Ironmak. Steelmak.* **2016**, *43*, 264–307. https://doi.org/10.1179/1743281215Y.0000000063.
37. Lagneborg, R.; Siwecki, T.; Zajac, S.; Hutchinson, B. Role of Vanadium in Microalloyed Steels. *Scand. J. Metall.* **1999**, *28*, 186–241.
38. Klinkenberg, C.; Hulka, K.; Bleck, W. Niobium Carbide Precipitation in Microalloyed Steel. *Steel Res. Int.* **2004**, *75*, 744–752. https://doi.org/10.1002/srin.200405837.
39. Karmakar, A.; Kundu, S.; Roy, S.; Neogy, S.; Srivastava, D.; Chakrabarti, D. Effect of Microalloying Elements on Austenite Grain Growth in Nb-Ti and Nb-V Steels. *Mater. Sci. Technol.* **2014**, *30*, 653–664. https://doi.org/10.1179/1743284713Y.0000000386.
40. Baker, T.N. Role of Zirconium in Microalloyed Steels: A Review. *Mater. Sci. Technol.* **2014**, *31*, 265–294. https://doi.org/10.1179/1743284714y.0000000549.
41. Graux, A.; Cazottes, S.; De Castro, D.; San Martín, D.; Capdevila, C.; Cabrera, J.M.; Molas, S.; Schreiber, S.; Mirković, D.; Danoix, F.; et al. Precipitation and Grain Growth Modelling in Ti-Nb Microalloyed Steels. *Materialia* **2019**, *5*, 100233. https://doi.org/10.1016/j.mtla.2019.100233.
42. Jung, J.G.; Park, J.S.; Kim, J.; Lee, Y.K. Carbide Precipitation Kinetics in Austenite of a Nb-Ti-V Microalloyed Steel. *Mater. Sci. Eng. A* **2011**, *528*, 5529–5535. https://doi.org/10.1016/j.msea.2011.03.086.
43. *AWS A4.2M:2020* (*ISO 8249:2018, MOD*); Standard Procedures for Calibrating Magnetic Instruments to Measure the Delta Ferrite Content of Austenitic and Duplex Ferritic-Austenitic Stainless Steel Weld Metal. American Welding Society: Miami, FL, USA, 2020.
44. Pokorný, J.; Kubásek, J.; Donik, Č.; Nečas, D.; Hybášek, V.; Fojt, J.; Dobkowska, A.; Paulin, I.; Čapek, J.; Godec, M. Enhanced Performance of Austenitic Oxide Dispersion-Strengthened 316L Steel: A Study on Y_2O_3 Reinforcement and Corrosion Behaviour. *Materials* **2025**, *18*, 641. https://doi.org/10.3390/ma18030641.
45. Zhao, W.; Wu, Y.; Jiang, S.; Wang, H.; Liu, X.; Lu, Z. Micro-Alloying Effects of Yttrium on Recrystallization Behavior of an Alumina-Forming Austenitic Stainless Steel. *J. Iron Steel Res. Int.* **2016**, *23*, 553–558. https://doi.org/10.1016/S1006-706X(16)30087-5.